Summer Students Italian Program at Fermilab

DUNE Photon Detection System: Single photo-electron rates in ProtoDUNE

Xenon doping of LAr

Niccolò Gallice

October 26, 2019

Contents

1 Dune

The Deep Underground Neutrino Experiment (DUNE) [1] will be a world-class neutrino observatory and nucleon decay detector designed to answer fundamental questions about the nature of elementary particles and their role in the universe. The international DUNE experiment, hosted by the U.S. Department of Energy's FNAL, will consist of a far detector to be located about 1.5 km underground at the Sanford Underground Research Facility (SURF) in South Dakota, USA, at a distance of 1300 km from FNAL, and a near detector to be located at FNAL in Illinois. The far detector will be a very large, modular liquid argon time-projection chamber (LArTPC) with a 40 kt fiducial mass. This LAr technology will make it possible to reconstruct neutrino interactions with image-like precision and unprecedented resolution.

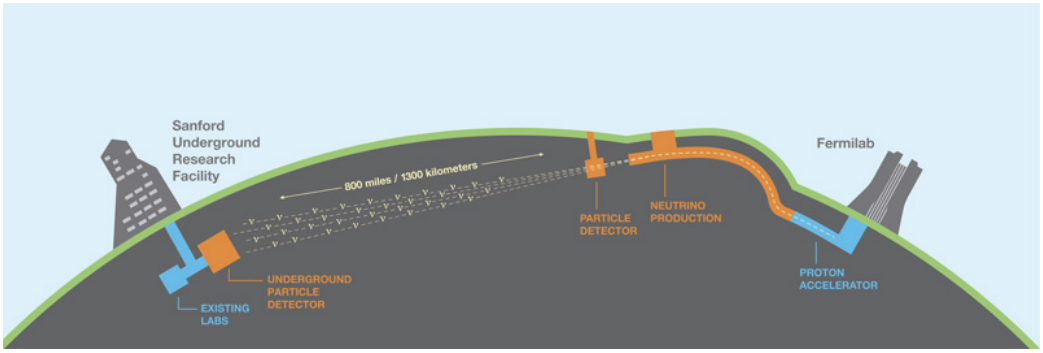

Figure 1: The DUNE experiment. A beam of ν produced at Fermilab is monitored by the near detector and sent to the far detector at 1300 km to study neutrino oscillation.

1.1 Long Baseline Neutrino Facility

The Long-Baseline Neutrino Facility (LBNF) is intended to enable the construction and operation of the DUNE detectors in South Dakota and Illinois. The DUNE collaboration will construct a deep-underground neutrino observatory in South Dakota based on four independent 10 kt LArTPCs. LBNF will provide facilities in Illinois and South Dakota to enable the scientific program of DUNE.

Specifically, the Long-Baseline Neutrino Facility (LBNF) provides

- the technical and conventional facilities for a powerful 1.2 MW neutrino beam utilizing the PIP-II upgrade of the Fermilab accelerator complex,

to become operational by 2026 at the latest, and to be upgradable to 2.4 MW with the proposed PIP-III upgrade;

- the civil construction, or conventional facility (CF), for the near detector systems at Fermilab; (see Figure 3);
- the excavation of four underground caverns at SURF, planned to be completed by 2021 under a single contract, with each cavern to be capable of housing a cryostat with a minimum 10 kt fiducial mass LArTPC; and
- surface, shaft, and underground infrastructure to support the outfitting of the caverns with four free-standing, steel-supported cryostats and the required cryogenics systems. The first cryostat will be available for filling, after installation of the detector components, by 2023, enabling a rapid deployment of the first two 10 kt far detector modules. The intention is to install the third and fourth cryostats as rapidly as funding will allow.

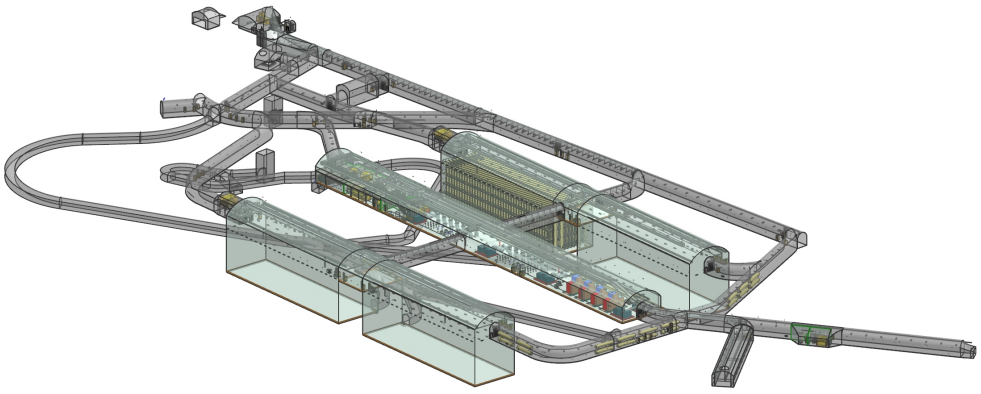

Figure 2: The far detector site is composed by four experimental rooms hosting LAr TPC.

The neutrino beam will consist of ν_μ or $\overline{\nu_\mu}$ and those will be selected using the positive or negative polarization of the focusing magnetic horns. The main observed oscillation channels will be $\nu_\mu \rightarrow \nu_\mathrm{e}$ or alternatively $\overline{\nu_\mu} \rightarrow \overline{\nu_\mathrm{e}}$. For the first channel the beam contamination will consist essentialy of $\overline{\nu_\mu}$ and ν_e, thus electron neutrinos will be the first cause of systematic error. The expected neutrino energy distribution shown in figure 4 on the following page will allow a good recognition of oscillation patterns (figure 5a on page 5) and mass hierarchy identification (figure 5b on page 5).

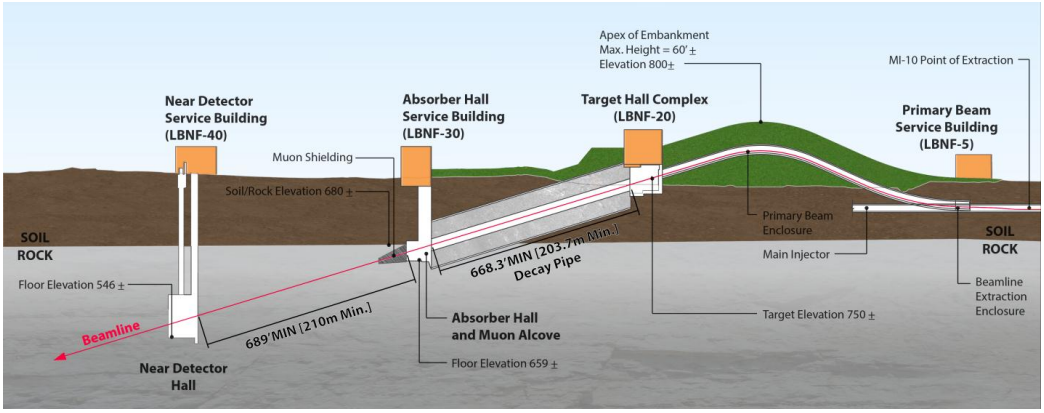

Figure 3: Neutrino beamline and DUNE near detector hall at Fermilab: neutrinos are produced in the decay pipe and then monitored by the near detector.

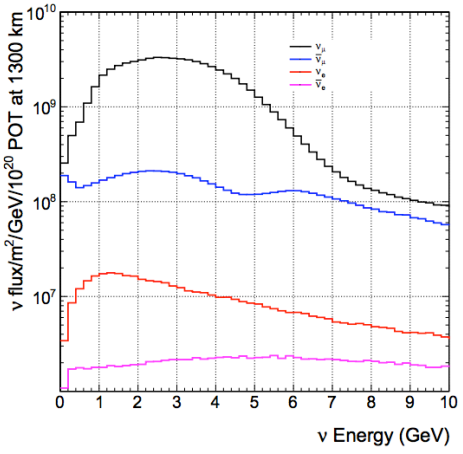

Figure 4: Expected neutrino flux at the far site for a ν_μ beam as a function of energy.

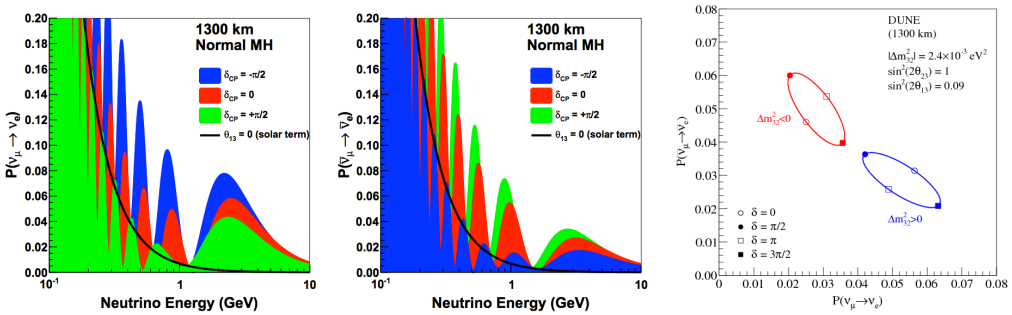

(a) (b)

Figure 5: On the left the oscillation pattern at 1300 km from neutrino beam generation as a function of energy. On the right the dependence of neutrino and antineutrino asimmetry for normal and inverted mass ordering.

1.2 DUNE far detector

The DUNE far detector will consist of four similar LArTPCs, each with fiducial mass of at least 10 kt, installed about 1.5 km underground. Each detector will be installed in a cryostat with internal dimensions 14.0 m (W) × 14.1 m (H) × 62.0 m (L), and will contain a total LAr mass of about 17.5 kt. The LArTPC technology provides excellent tracking and calorimetry performance, making it an ideal choice for the DUNE far detectors. The four identically sized cryostats give flexibility for staging and evolution of the LArTPC technology.

DUNE is planning for and prototyping two LArTPC technologies:

- Single-phase (SP): This technology was pioneered by the ICARUS project, and after several decades of worldwide R&D, is now a mature technology. It is the technology used for Fermilab's currently operating MicroBooNE, and the planned SBND. In the single-phase technology, ionization charges are drifted horizontally in LAr and read out on wires in the liquid. The maximum drift length in the DUNE single-phase module is 3.53 m and the nominal drift field is 500 V cm^{-1}, corresponding to a cathode high voltage of 180 kV. There is no signal amplification in the liquid, so readout with good signal-to-noise requires very low-noise electronics.

- Dual-phase (DP): This technology was pioneered at large scale by the WA105 collaboration. It is less established than the single-phase technology but offers a number of potential advantages and challenges.

Here, ionization charges are drifted vertically in Lar and transferred into the gas above the liquid. The signal charges are then amplified in the gas phase using large electron multipliers (LEMs). This gain reduces the requirements on the electronics, and makes it possible for the dual-phase module to have a longer drift, which requires a correspondingly higher voltage. The maximum drift length in the DP module is 12 m and the nominal drift field is $500\,\mathrm{V\,cm^{-1}}$, corresponding to a cathode high voltage of 600 kV.

1.3 Physics goals

The primary science program of DUNE [2] focuses on fundamental open issues in neutrino and astroparticle physics:

- Precision measurements of the parameters that govern $\nu_\mu \rightarrow \nu_\mathrm{e}$ and $\overline{\nu}_\mu \rightarrow \overline{\nu}_\mathrm{e}$ oscillations with the goal of

  – measuring the charge-parity (CP) violating phase δ_CP, where a value differing from zero or π would represent the discovery of CP violation in the leptonic sector, providing a possible explanation for the matter-antimatter asymmetry in the universe;

  – determining the neutrino mass ordering (the sign of $\Delta m^2_{31} \equiv m^2_3 - m^2_1$), often referred to as the neutrino *mass hierarchy*; and

  – precision tests of the three-flavor neutrino oscillation paradigm through studies of muon neutrino disappearance and electron neutrino appearance in both ν_μ and $\overline{\nu}_\mu$ beams, including the measurement of the mixing angle θ_{23} and the determination of the octant in which this angle lies.

- Search for proton decay in several important decay modes. The observation of proton decay would represent a ground-breaking discovery in physics, providing a portal to Grand Unification of the forces; and

- Detection and measurement of the ν_e flux from a core-collapse supernova within our galaxy, should one occur during the lifetime of the DUNE experiment.

1.3.1 CP violation

DUNE will search for CP violation using the ν_μ to ν_e and $\overline{\nu_\mu}$ to $\overline{\nu_e}$ oscillation channels, with two objectives. First, DUNE aims to observe a signal for leptonic CP violation independent of the underlying nature of neutrino

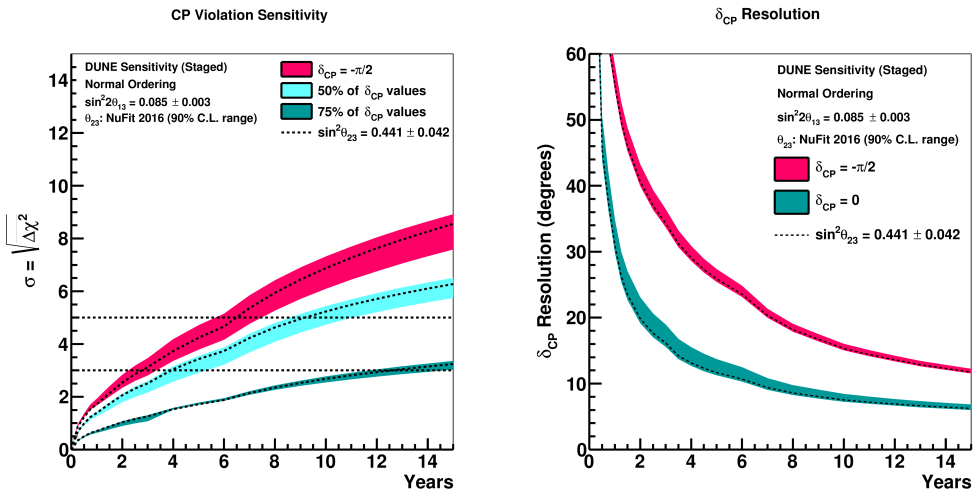

Figure 6: The significance with which CP violation can be determined for 75% and 50% of $\delta_{\rm CP}$ values and for $\delta_{\rm CP}$=-$\pi/2$ (left) and the expected 1σ resolution (right) as a function of exposure in years using the proposed staging plan outlined in this chapter. The shaded regions represent the range in sensitivity corresponding to different true values of θ_{23}. The plots assume normal mass hierarchy.

oscillation phenomenology. Such a signal will be observable in comparisons of $\nu_\mu \to \nu_e$ and $\bar{\nu}_\mu \to \bar{\nu}_e$ oscillations of the LBNF beam neutrinos in a wide range of neutrino energies over the 1300 km baseline. Second, DUNE aims to make a precise determination of the value of $\delta_{\rm CP}$ within the context of the standard three-flavor mixing scenario described by the PMNS neutrino mixing matrix.

Figure 6 shows, as a function of time, the expected sensitivity to CP violation expressed as the minimum significance with which CP violation can be determined for 75% and 50% of $\delta_{\rm CP}$ values as well as the sensitivity when the true value of $\delta_{\rm CP}$=-$\pi/2$. Also shown is the 1σ resolution for $\delta_{\rm CP}$ as a function of time for $\delta_{\rm CP} = 0$ (no CP violation) and $\delta_{\rm CP} = -90°$ (maximal CP violation). In both figures the staging scenario described previously is assumed. The exposure required to measure $\delta_{\rm CP} = 0$ with a precision better than 10° is 250 kt MW year or about six and a half years of operation. A full-scope LBNF/DUNE operating with multi-megawatt beam power can in time achieve a precision comparable to the current precision on the CP phase in the CKM matrix in the quark sector (5%).

1.3.2 Mass hierarchy

While significant progress on mass hierarchy (MS) estimation is expected from currently running experiments, DUNE's ability to resolve the MH for all allowed values of mixing parameters is a key strength.

The discriminating power between the two MH hypotheses is quantified by the difference, denoted $\Delta\chi^2$, between the $-2\log\mathcal{L}$ values calculated for the normal and inverted hierarchies. As the sensitivity depends on the true value of the unknown CP-violating phase, $\delta_{\rm CP}$, all possible values of $\delta_{\rm CP}$ are considered. In terms of this test statistic[1], the MH sensitivity of DUNE for exposures of seven and ten years is illustrated in Figure 7 for the case of normal hierarchy and the NuFit 2016 [3] best-fit value of $\sin^2\theta_{23} = 0.44$. For this exposure, the DUNE determination of the mass hierarchy will be definitive for the overwhelming majority of the $\delta_{\rm CP}$ and $\sin^2\theta_{23}$ parameter space. Even for unfavorable combinations of the parameters, a statistically ambiguous outcome is highly unlikely.

Figure 7 shows the evolution of the sensitivity to the mass hierarchy determination as a function of years of operation, for the least favorable scenario (blue band), corresponding to the case in which the MH asymmetry is maximally offset by the leptonic CP asymmetry. An exposure of 209 kt MW year (which corresponds to approximately five years of operation) is required to distinguish between normal and inverted hierarchy with $|\Delta\chi^2| = \overline{|\Delta\chi^2|} = 25$. This corresponds to a $\geq 99.9996\%$ probability of determining the correct hierarchy.

1.3.3 Nucleon decay

Unification of three of the fundamental forces in the universe, the strong, electromagnetic and weak interactions, is a central paradigm for the current world-wide program in particle physics. Grand Unified Theories (GUTs), aiming at extending the standard model of particle physics to include a unified force at very high energies (above 10^{15} GeV), predict a number of observable effects at low energies, such as nucleon decay [4, 5, 6]. Several experiments have been searching for signatures of nucleon decay, with the best limits for most decay modes set by the Super-Kamiokande experiment [7], which features the largest sensitive mass to date.

The DUNE far detector, as the largest active volume of argon, will be highly sensitive to a number of possible nucleon decay modes, in many cases

[1]For the case of the MH determination, the usual association of this test statistic with a χ^2 distribution for one degree of freedom is not strictly correct; additionally the assumption of a Gaussian probability density implicit in this notation is not exact.

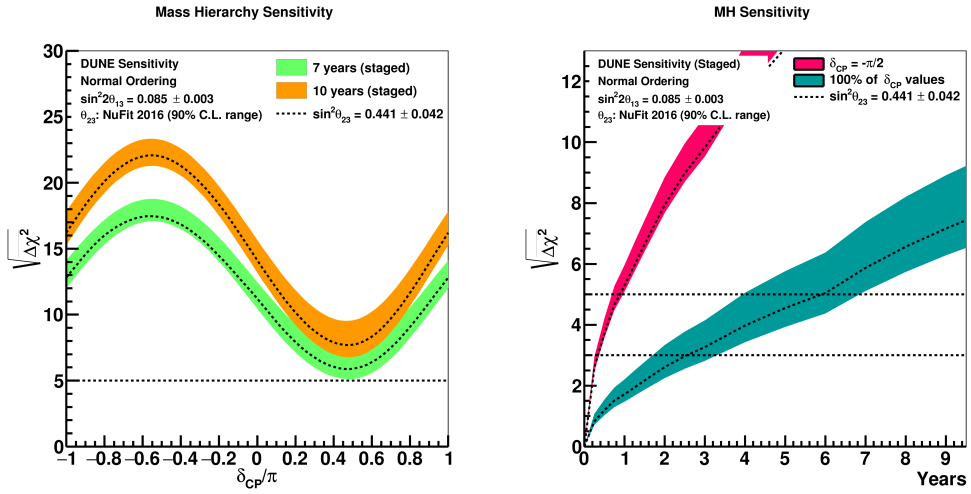

Figure 7: The square root of the mass hierarchy discrimination metric $\Delta\chi^2$ is plotted as a function of the unknown value of $\delta_{\rm CP}$ for exposures of seven and ten years (left). The minimum significance – the lowest point on the curve on the left – with which the mass hierarchy can be determined for all values of $\delta_{\rm CP}$ and the significance for a true value of $\delta_{\rm CP}$=-$\pi/2$ as a function of years of running under the staging plan described in the text (right). The shaded regions represent the range in sensitivity corresponding to different true values of θ_{23}.

complementing the capabilities of large water detectors. In particular, the LArTPC technology is expected to be well-suited for observing nucleon decays into charged kaons, which can be identified with redundancy from their distinctive dE/dx signature as well as by their decays.

As is the case for the entire non-accelerator based physics program of DUNE, nucleon decay searches require efficient triggering and event localization (within the far detector) capabilities. Given the 1 GeV energy release, the requirements on tracking and calorimetry capabilities are similar to those for the beam-based neutrino oscillation program described in the previous section. Experimental challenges such as particle identification to separate protons from kaons, the impact of final state interactions (FSI) on proton decay kinematics, and full control of the potential background processes, are presently under study with realistic detector simulations. This includes opportunities for enhanced background rejection by using convolutional neural networks, as well as efforts to understand the uncertainty associated with the intra-nuclear cascade model used to simulate FSI. We expect that ProtoDUNE data taken with charged particle beams at CERN will provide important sample of events to train and improve on reconstruction algorithms and the resulting dE/dx resolution.

Baryon number non-conservation can also be manifested by neutron-antineutron oscillations leading to subsequent antineutron annihilation with a neutron or a proton. This annihilation event will have a distinct signature of a vertex with several emitted light hadrons, with total energy of twice the nucleon mass and net momentum zero. More information about particle identification and energy measurements will be provided by the ProtoDUNE experiment with charged particle beams.

1.3.4 Supernova Neutrino Burst

The neutrinos from a core-collapse supernova are emitted in a burst of a few tens of seconds duration, with about half the signal emitted in the first second. The neutrino energies are mostly in the range 5 to 50MeV, and the flux is divided roughly equally between the three known neutrino flavors. Current water and scintillator detectors are sensitive primarily to electron antineutrinos ($\bar{\nu}_e$), with detection through the inverse-beta decay process on free protons, which dominates the interaction rate in these detectors. Liquid argon has a unique sensitivity to the electron-neutrino (ν_e) component of the flux, via the absorption interaction on ^{40}Ar,

$$\nu_e + {}^{40}\mathrm{Ar} \;\rightarrow\; e^- + {}^{40}\mathrm{K}^*.$$

Observation of the core-collapse neutrino burst in DUNE will provide crit-

ical information on key astrophysical phenomena [8]. Furthermore, detection of the supernova burst neutrino signal in DUNE will provide information on neutrino properties: see reference [8]. Most notably, several features offer multiple signatures of mass ordering [9], likely the most robust being the level of suppression of the neutronization burst: see Figure 8. Because the neutronization burst is ν_e-rich, this mass ordering signature is especially clean in DUNE.

Because no beam trigger is available for a supernova, efficient triggering and continuous data collection is critical for supernova neutrino burst physics. To fully capitalize on the physics opportunities, the DUNE far detector must provide event timing capability at the sub-millisecond level, must have spatial readout granularity sufficient to track electrons down to 5 MeV with good energy resolution, and must operate at noise levels and thresholds that allow detection and energy measurement for deexcitation gammas and nucleons at the MeV level. The LArTPCtechnologies underlying the DUNE far detector conceptual designs is capable of meeting these requirements.

We note that information from DUNE will be highly complementary with neutrino burst information from other detectors, and furthermore multi-messenger astronomy information (from gravitational waves and a broad range of electromagnetic wavelengths) will combine to provide a full picture of a core-collapse event.

1.4 DUNE photon detection system

LAr is an excellent scintillating medium and the photon detection system (PDS) is used to obtain additional event information from the photons produced by particles traversing the detector. With an average energy of 19.5 eV needed to produce a photon (at zero field), a typical particle depositing 1 MeV in LAr generates 40 000 photons with a wavelength of 128 nm. In higher electric fields this number is reduced, but at 500 V/cm the yield is still $\sim$ 20000 photons per MeV. Roughly 1/4 of the photons are promptly emitted with a lifetime of about 6 ns, while the rest are produced with a lifetime of 1100 ns to 1600 ns. Prompt and delayed photons are detected in precisely the same way by the photon detection system. LAr is highly transparent to the 128 nm VUV photons with a Rayleigh scattering length of (66 ± 3) cm [11] and absorption length of > 200 cm; assuming a LN2 content of less than 20 ppm. Many of the objectives require a TPC with a high performance in calorimetric and space-time measurements, such goals wouldn't be reached without the use of a highly performant Photon Detection System (PDS). In particular the PDS will be essential for nucleon decay searches, being the sole instrument to localize the events in the TPC. It will also enhance results in different physics

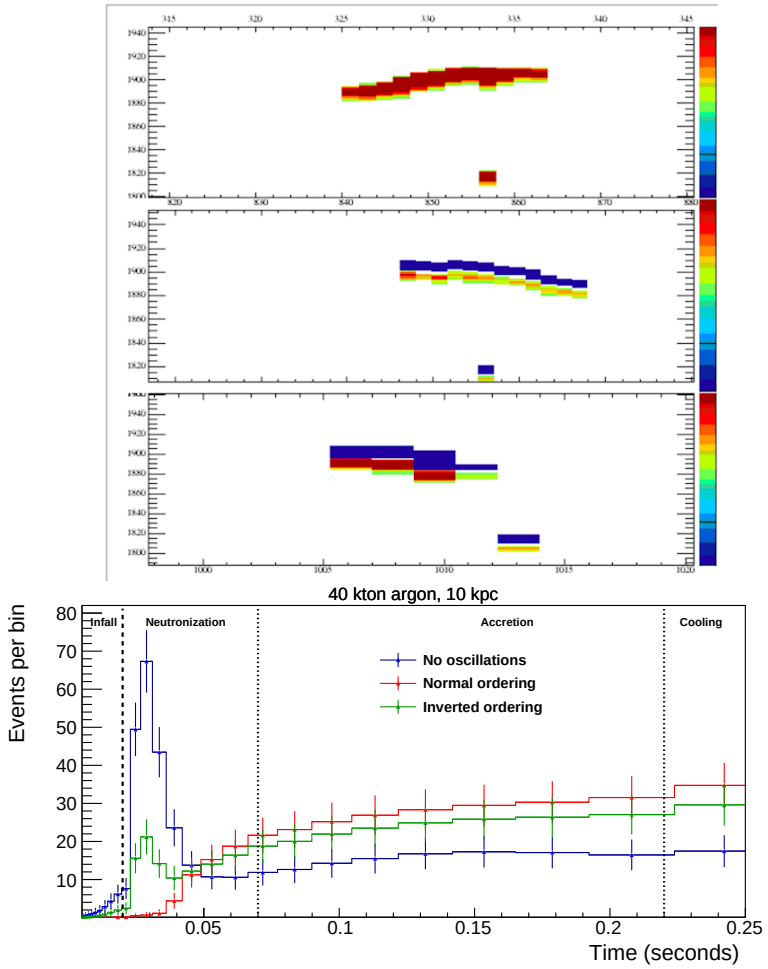

Figure 8: Top: Event display of a 30 MeV neutrino event simulated using MARLEY (Model of Argon Reaction Low-Energy Yields). Bottom: Expected event rates as a function of time for the electron-capture SNB model in [10] for 40 kt of argon during early stages of the event – the neutronization burst and early accretion phases. Shown is the event rate for the unrealistic case of no flavor transitions (blue), the event rate including the effect of matter transitions for the normal (red) and inverted (green) hierarchies. Error bars are statistical, in unequal time bins.

areas: the increase of reliability of vertex position reconstruction and calorimetric improvement will bring sensitivity to the underlying models for SNB, improve resolution and provide reconstruction redundancy for beam neutrino events, and open up the investigation of few-MeV scale solar neutrinos.

2 ProtoDUNE

ProtoDUNE-SP is the single-phase DUNE Far Detector prototype that is operating at CERN. It is an important step to the 17 kt TPC of the final detector as it represents the largest monolithic single-phase LArTPC detector to be built to date. ProtoDUNE-SP prototypes the designs of most of the single-phase DUNE far detector module (DUNE-SP) components at a 1:1 scale, with an extrapolation of about 1:20 in total LAr mass (0.77 kt). The construction and operation of ProtoDUNE-SP is used to validate the membrane cryostat technology and associated cryogenics, and the networking and computing infrastructure that will handle the data and simulated data sets. A charged-particle beam test enables critical calibration measurements necessary for precise calorimetry. It has also made possible the collection of invaluable data sets for optimizing the event reconstruction algorithms – i.e., for finding interaction vertices and for particle identification – and ultimately for quantifying and reducing systematic uncertainties for the DUNE far detector. These measurements are expected to significantly improve the physics reach of the DUNE experiment [11].

The ProtoDUNE detector (figure 9 on the next page) is shown from the "Rack" side, exposing part of the beam upstream face. The charge readout is composed by 6 anode planes (APA) and 1 cathode plane (CPA) positioned in the middle at 3.6 m from detector sides. Each anode plane consists of a wire structure and photon detection modules installed horizontally. The APAs are three for each side and are named according to their installation side as "Rack" (front side of figure) and "DAQ" (opposite side). The horizontal position is given with respect to the beam, thus the left APA is called upstream, the one in the middle middlestream and the right APA downstream. According to ProtoDUNE naming the APA #3 of figure 9 on the following page is named UsRaS, which stands for upstream rack side, the APA #2 MsRaS and the APA #1 DsRaS.

3 Photon detection system

The ProtoDUNE Photon Detection System consist of:

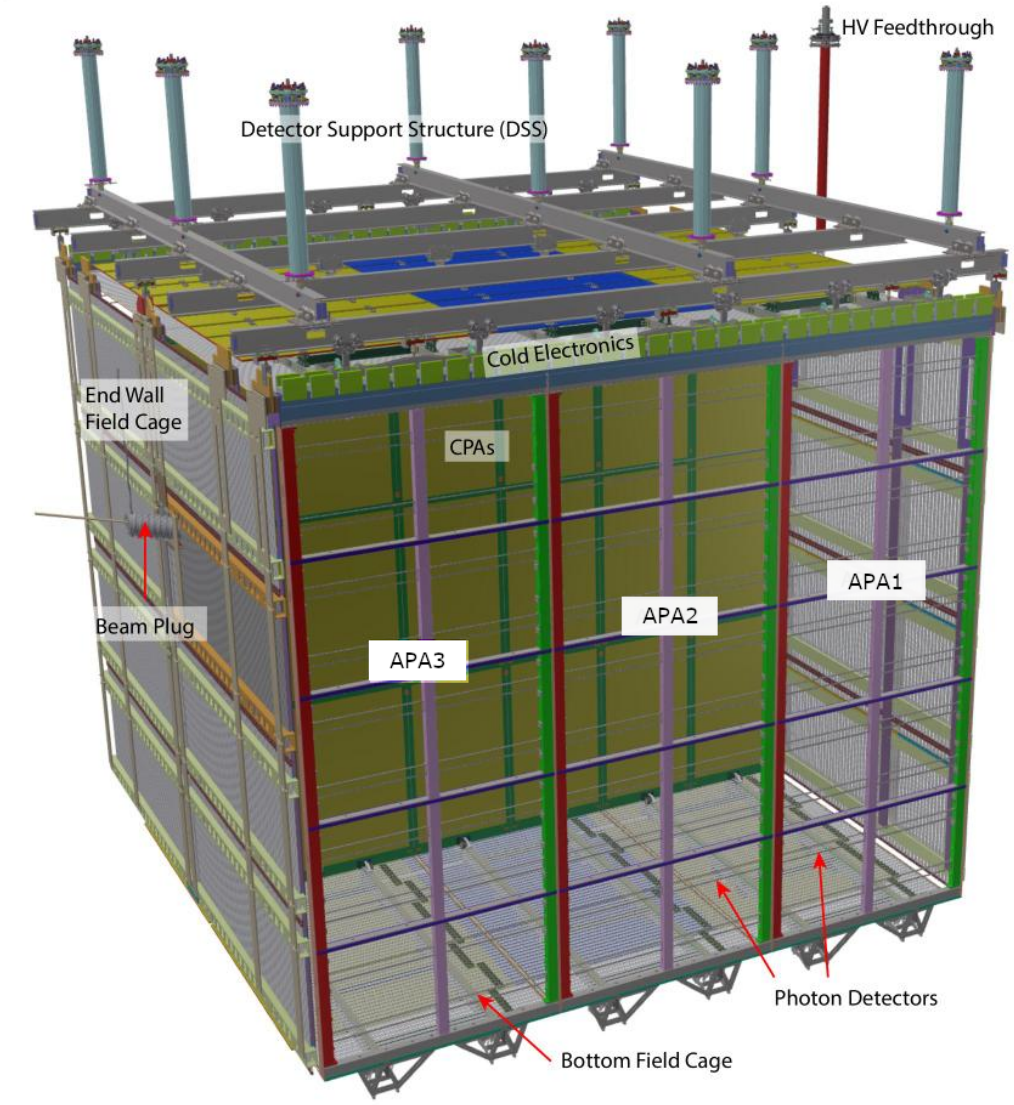

Figure 9: Scheme of ProtoDUNE-SP. On the front side (Rack side) three anode planes are installed, in the middle the cathode plane, while on the opposite side (DAQ side) other three anode planes. Each anode plane lays at 3.6 m from the cathode and consists of a wire structure and photon detection modules installed horizontally. The APA on the Rack side are named UsRaS (Upstream Rack Side), MsRaS (Midstream Rack Side) and DsRaS (Downstream Rack Side) going from beam side to the other end. Similarly on the DAQ side the names are UsDaS, MsDaS and DsDaS. The beam reaches the detector from the left side.

- Light collection systems
- Light sensors: Silicon Photo-Multipliers (SiPM)
- Readout electronics
- Monitoring System

Three types of PDS modules are installed in ProtoDUNE-SP, the first two are very similar and differ only for the number of times light is shifted, while the last one is specifically developed for DUNE and is called ARAPUCA.

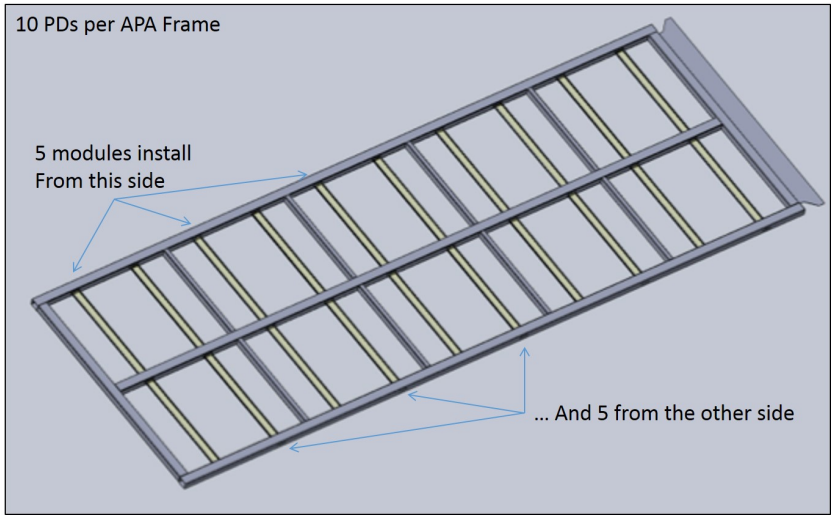

Figure 10: Installation of photon detector modules inside an anode plane (APA).

In the propotyopes two different models of Silicon Photo-Multipliers are installed. The SensL C-Series 6 mm^2 (MicroFB-60035-SMT) are used for WLS bar, while Hamamatsu S13360 is mounted inside the ARAPUCA modules.

To calibrate and monitor the PDS, 10 LEDs with optical fiber are installed in ProtoDUNE-SP, their purpose is to give a tunable source of light to understand the response of the sensors and to check their time stability.

3.1 Wavelenght shifting bars

The first solution (figure 11 on the next page) is composed of wavelenght-shifting radiator plates coated with tetraphenyl-butadiene (TPB) to produce

blue light (430 nm), mounted on commercially produced wavelength shifting (WLS) polystyrene bar with Y-11 fluor, producing green light, which is transmitted through the light guide to the photosensor installed at its end.

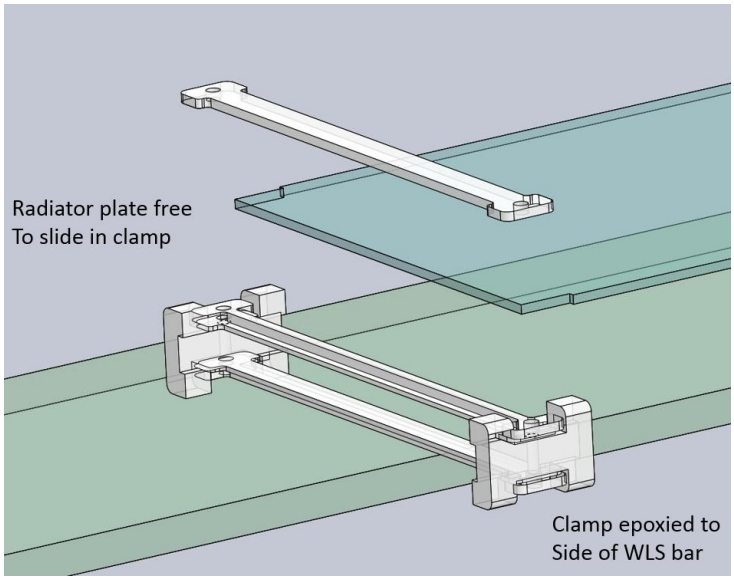

Figure 11: First kind of wavelength shifting collector. Mounting of a radiator plate on a wavelength shifting light guide.

The second solution (figure 12 on the following page)) is very similar although no radiator is present. The WLS bars are coated with a solution of TPB, solvents, and a surfactant to produce a wavelength-shifting layer on the outside surface of the bar. The 128 nm light is then converted to the blue spectrum and detected by the SiPM installed at the end of the bar.

3.2 ARAPUCA

The ARAPUCA [12] is the baseline photon detector module for DUNE. It has been developed specifically for this experiment to increase the light collection efficiency of the system while limiting the active coverage of SiPMs.

The idea of ARAPUCA is to trap photons inside a box with highly reflective surfaces until it is detected by a SiPM. For this purpose, the box (figure 13 on page 18) has one open side where a dichroic filter is installed. The working principle of the dichroic filter is to create a short-pass filter in order to be transparent under a threshold wavelength. The photons which entered the box, must have a wavelength greater than the filter threshold to be trapped. To this end, the filter is coated with wavelength shifters on the two sides.

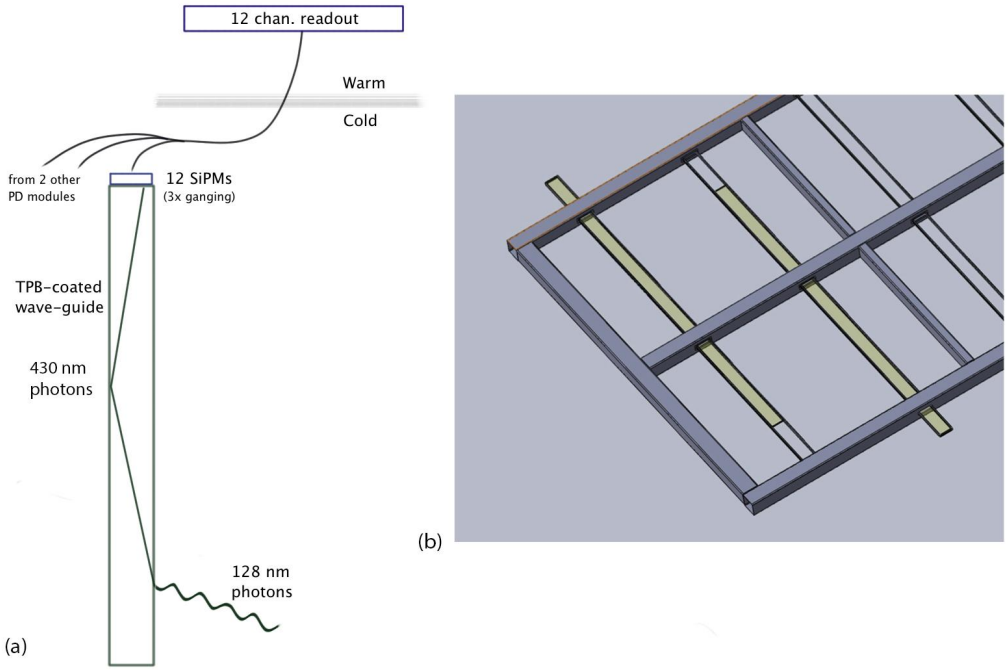

Figure 12: On the left, the scheme of the second type of light collector, consisting of TPB coated wave guide. On the right, the installation of such technology inside an APA.

The shifters deposited on the two faces of the dichroic filter (figure 13), S_1 and S_2 respectively, must have their emission wavelengths, L_1 and L_2, such that: $L_1 < L_{\text{cut-off}} < L_2$, where $L_{\text{cut-off}}$ is the cut-off wavelength of the filter, that is the limit between the region of full transparency (typically $> 95\,\%$) and that of full reflectivity (typically $98\,\%$). The side of the filter deposited with S_2 faces the internal part of the box.

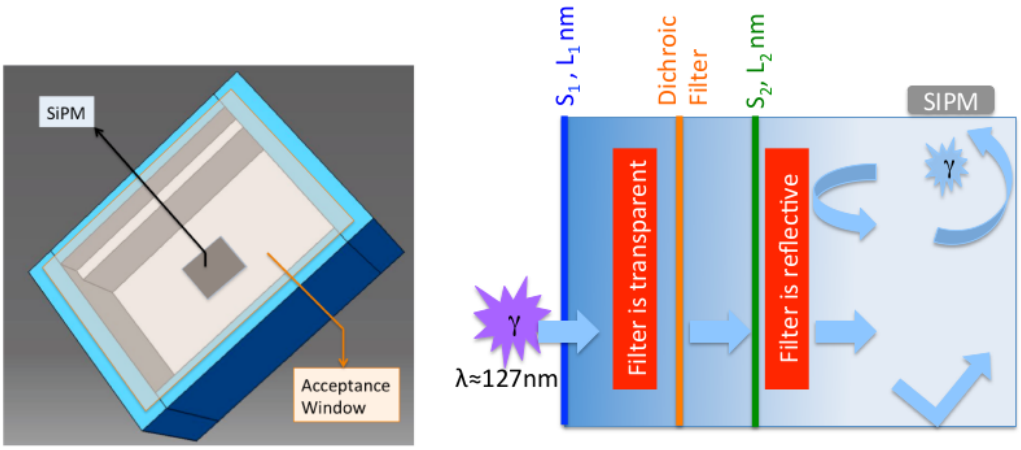

Figure 13: On the left, the ARAPUCA box with reflective surfaces and a SiPM installed at its bottom. On the right the working principle of ARAPUCA: the 127 nm light is shifted at S_1, passes through the dichroic filter and is shifted again at S_2. At this point the photon is trapped until its detection.

The external surface of the filter is coated with p-terphenyl (PTP) with an emission wavelength or 350 nm, while the shifter deposited on the internal side is Tetraphenyl-butadiene (TPB) with an emission wavelength of 430 nm. The expected response of the filter is presented in figure 14 on the next page: on the left the TPB emission spectrum is compared to the reflectivity of the filter, while on the right the emission of PTP is compared to the transmission efficiency.

The light impinging on the ARAPUCA window is first absorbed by TPB and emitted isotropically, thus just half of the light will cross the filter resulting in a $\epsilon_{PTP}/2$ efficiency. On the other hand the shifting efficiency of PTP is $\epsilon_{TPB} \sim 80\,\%$. The total efficiency of the window is given by $\epsilon_W = \epsilon_{PTP}/2 \times T_w \times \epsilon_{TPB} \sim 1/3$ where the transmission efficiency of the dichroic filter T_w is taken into account.

The efficiency of the system can be estimated considering the window efficiency ϵ_W, thus the probabilty that a photon enters the box, and the

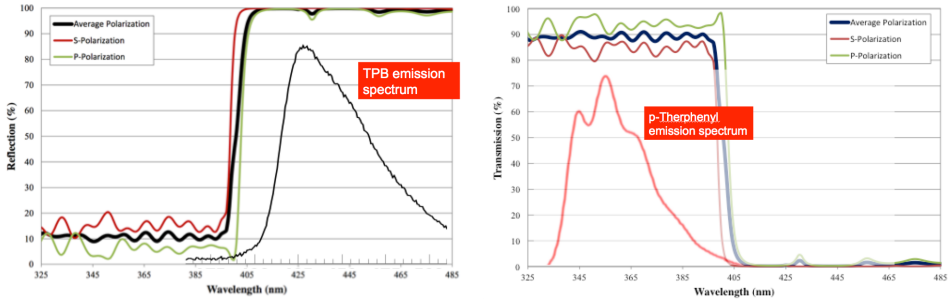

(a) (b)

Figure 14: In figure (a) the reflectivity of the dichroic filter is matched to the TPB emission spectrum. In figure (b) the transmission coefficient is compared to the emission spectrum of PTP.

collection efficiency ϵ_{coll}, thus the probability that a photon is collected by the SiPM. The collection efficiency given by equation 1. Where f is the fraction of internal surface covered with light sensors and R_w the reflectivity of internal walls. This quantity is the probability that a photon in the box is collected by the SiPM.

$$\epsilon_{coll} = \frac{f}{1 - R_W(1 - f)} \tag{1}$$

The total efficiency of the system is thus

$$\epsilon_{tot} = \epsilon_w \times \epsilon_{coll} \times \epsilon_{SiPM} \tag{2}$$

For $f = 0.1\,\%$ it results in a collection efficiency $\epsilon_{coll} \sim 4.8\,\%$. Considering a box of 25 cm side and a $0.1\,\%$ coverage corresponds to an active SiPM area of $\sim (1.1 \times 1.1)$ cm^2. Considering a photon detection efficiency for SiPMs around $60\,\%$, the total efficiency for such a system is around $1\,\%$.

4 Single Photon Rate in LAr TPC

Liquid Argon time projection chambers located at ground level show a high single photon rate. In particular μBoone has been a test stand for the confirmation of this phenomenon. Although the cause of this behavior is not completely clear it can be correlated with the formation of a ion space-charge induced by a high rate of cosmic rays. At the moment ProtoDUNE single phase is the largest TPC that is located at ground level and it can be used to deeply understand the process underlying the single photon rate that is observed. Its long drift distance 3.5 m should enhance the space charge formation and thus the single photon rate. Furthermore the study of this variable with respect to the TPC parameters (cathode voltage, purity and time) could give hints about the causes of this phenomenon.

4.1 Light production in LAr

When a muon crosses the TPC it ionizes the liquid argon releasing energy in the medium. The Ar atom can use the energy to both go in an excited state Ar^* or to create a ion-electron couple $(Ar^+ - e^-)$. In the first case, the excited atom can collide with other non-excited atoms to create a molecule in a given excited state. The latter Ar_2^* can deexcite emitting one photon or interacting with an impurity being quenched. Considering the $Ar^+ - e^-$ those can recombine forming an excited state Ar^{**} that will end up in a Ar^* state that can produce one photon through deexcitetion. If the ion and electron don't undergo any of these processes they will continue drifting until they reach the cathode and anode respectively. The process is described in figure 15 on the next page.

The light emission is a fast process that takes place in the ns $\div$ µs range. The drifting of charges has a time scale that ranges from ms for electrons to 20 min for ions. If the rate of ionizing particles is high enough, ions will accumulate at the cathode creating a positive space charge as shown in figure 16 on the following page.

The positive ions that accumulate at the cathode in the steady state condition, create the space charge. These ions can eventually recombine with free negative elements creating a single photon.

4.2 SPR model

To compute the expected behavior of the single photon rate, it is important to understand the characteristics of space-charge. To this end the ion transport equations are considered.

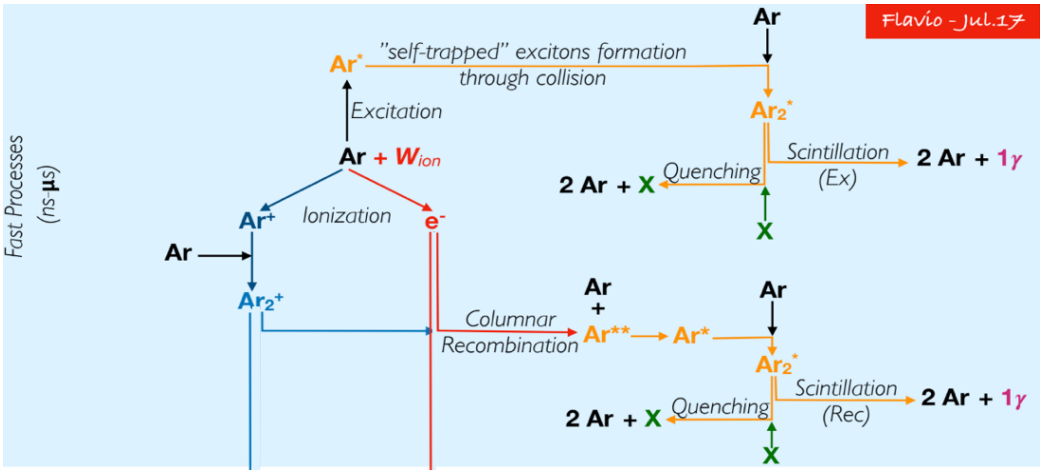

Figure 15: Fast processes that take place in the ionization of liquid argon. When the particle release an amount of energy in LAr the atom can go in an excited state Ar^* or to be ionized in $Ar^+ - -e^-$. In the first case through collision $Ar + Ar^* \rightarrow Ar_2^*$ that can eventually emit light. On the other hand the argon ion can interact Ar atoms $Ar^+ + Ar \rightarrow Ar_2^+$ and recombining with electrons $Ar_2^+ + e^- \rightarrow Ar^{**}$. At the end the molecule ends in the same state of the other process $Ar^{**} + Ar \rightarrow Ar_2^*$.

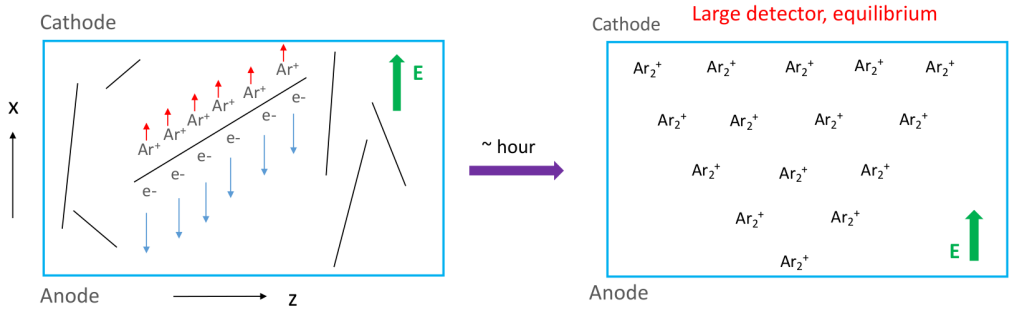

Figure 16: When a charged particle passes through liquid argon its deposited energy creates ionization (left). The charge that doesn't recombine starts drifting and electrons are 100000 times faster than ions. At the steady state argon ions Ar_2^+ will accumulate at the cathode surface creating a space-charge.

$$\begin{cases} \frac{\partial J_{e^-}}{\partial x} = S_{gen}(e^-) - S_{loss}(e^-) \\ \frac{\partial J_{I^+}}{\partial x} = S_{gen}(I^+) - S_{loss}(I^+) \end{cases} \tag{3}$$

In the case of ionization only the equations becomes:

$$\begin{cases} \frac{\partial(-\mu_e E n_e)}{\partial x} = n_{pair} \\ \frac{\partial(-\mu_+ E n_+)}{\partial x} = n_{pair} \\ \frac{\partial E}{\partial x} = \frac{1}{\epsilon}(n_+ - n_e) \end{cases} \tag{4}$$

where n_e is the concentration of electrons while n_+ the one of ions. On the other hand n_{pair} is the rate of creation of ion-electron couples after the first recombination that gives prompt light. The μ parameter is the mobility. The last equation is just the Gauss equation to constraint the electric field.

The system of differential equation is solved numerically considering $n_{pair} = 1.9 \times 10^9\,\mathrm{m^{-3}s^{-1}}$, $\mu_+ = 8 \times 10^{-8}\,^2\mathrm{mV^{-1}s^{-1}}$ and a cosmic rate $R = 13\,\mathrm{kHz}$. The result is plotted in figure 17.

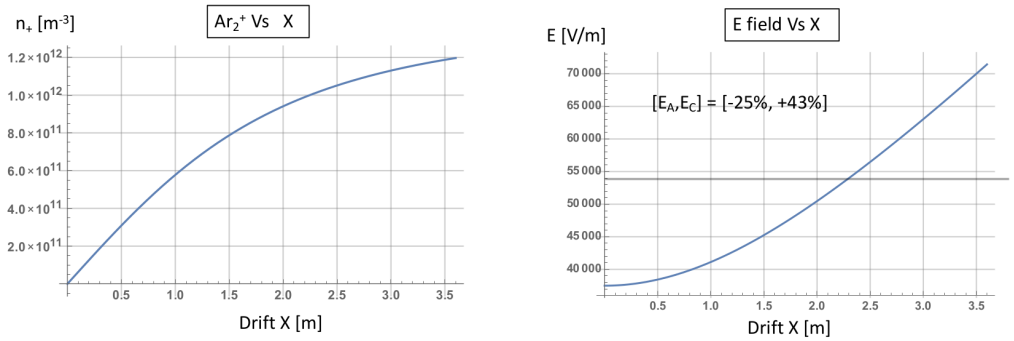

Figure 17: Model of ionization mechanism. On the left the concentration of ions with respect to the position, on the right the distortion of the electric field in the TPC caused by the space-charge.

Another possible process to include is the attachment of electrons to impurities. Electrons while drifting can be captured by impurities (H_2O, O_2, ...) thus creating negative ions that can drift too. In this case equations become:

$$\begin{cases} -\mu_e n_e \frac{\partial E}{\partial x} - v_d^e \frac{\partial n_e}{\partial x} = n_{pair} - k_A n_X n_e \\ -\mu_+ n_+ \frac{\partial E}{\partial x} - v_d^+ \frac{\partial n_+}{\partial x} = n_{pair} \\ -\mu_- n_- \frac{\partial E}{\partial x} - v_d^- \frac{\partial n_-}{\partial x} = k_A n_X n_e \\ \frac{\partial E}{\partial x} = \frac{1}{\epsilon}(n_+ - n_- - n_e) \end{cases} \tag{5}$$

where it was added the attachment rate k_A and the transport equation for negative ions (impuritiy–electron) n_-. The solution is obtained numerically considering a concetration of H_2O around 3 ppt (6 ms electron lifetime) and $k_A = 1.4 \times 10^{-15}\,\mathrm{m^3 s^{-1}}$. The figure 18 show the solution for the concetration of ionized impurities and the electric field inside the TPC.

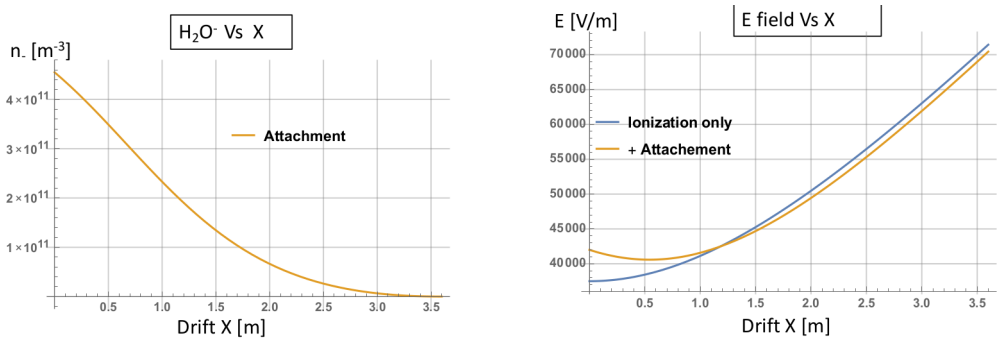

Figure 18: Model of impurity attachment: electrons can be captured by electronegative impurities. On the left the concentration of negative ions, while on the right the deformation of the electric field with the attachment process.

Adding the generation of ionized impurities implies also the possibility of their recombination. A new recombination process is taken into account: the "mutual neutralization", where an ionized impurity such as O_2^- recombines with a liquid argon ion Ar_2^+. An example is shown in figure 19.

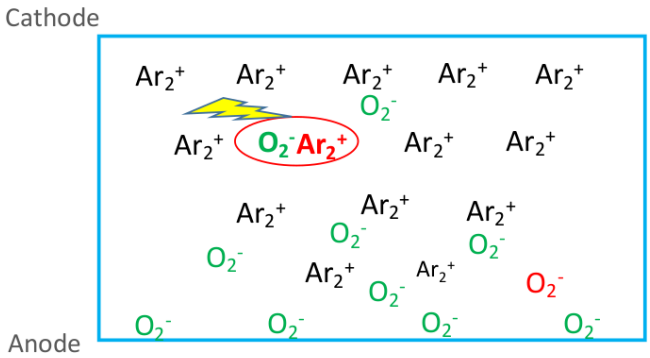

Figure 19: Mutual recombination mechanism: impurities that have trapped a free electron can recombine with argon ions emitting one photon.

In this case the equation modifies adding a loss term for positive and negative ions.

$$\begin{cases} -\mu_e n_e \frac{\partial E}{\partial x} - v_d^e \frac{\partial n_e}{\partial x} = n_{pair} - k_A n_X n_e \\ -\mu_+ n_+ \frac{\partial E}{\partial x} - v_d^+ \frac{\partial n_+}{\partial x} = n_{pair} - k_{MN} n_+ n_- \\ -\mu_- n_- \frac{\partial E}{\partial x} - v_d^- \frac{\partial n_-}{\partial x} = k_A n_X n_e - k_{MN} n_+ n_- \\ \frac{\partial E}{\partial x} = \frac{1}{\epsilon}(n_+ - n_- - n_e) \end{cases} \tag{6}$$

where k_{MN} gives the mutual neutralization rate. The solution to this case is given by the plots in figure 20. The rate of photons is given by the neutralization of ions $I^- + I^+ \rightarrow \gamma$.

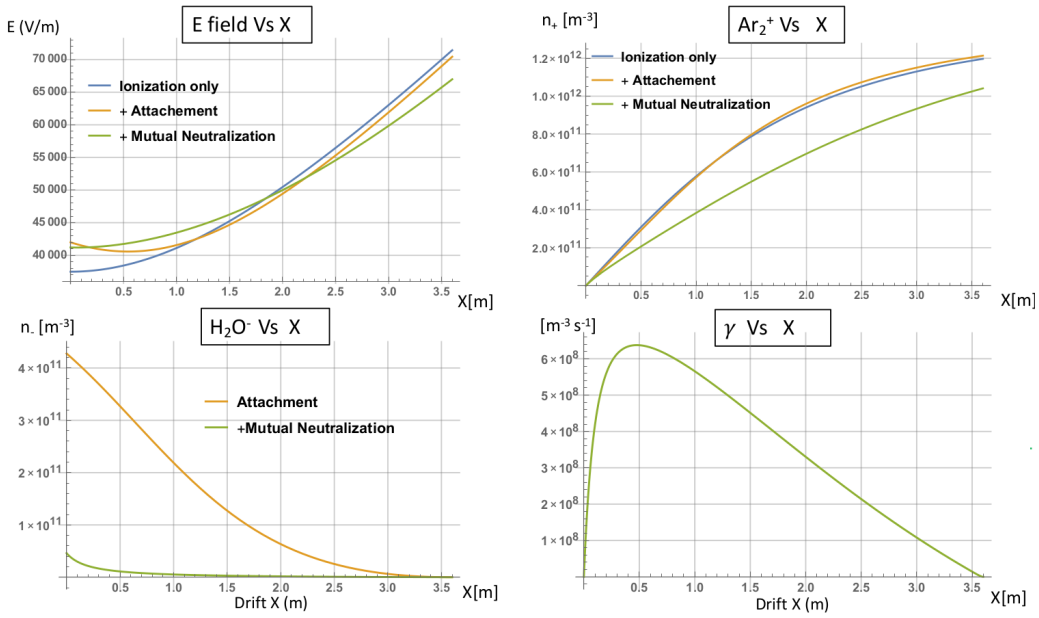

Figure 20: Solution of the model including ionization, attachment and mutual neutralization. On upper left the electric field distortion in the chamber, on the upper right the concentration of argon ions, on bottom left the concentration of negative ions. On bottom right the expected rate of photons generated by mutual neutralization with respect to the position in the TPC.

To complete the model it is necessary to consider the usual volume recombination process where electrons recombine with argon ions. Thus the final equations for the model are:

$$\begin{cases} -\mu_e n_e \frac{\partial E}{\partial x} - v_d^e \frac{\partial n_e}{\partial x} = n_{pair} - k_A n_X n_e - k_R n_+ n_e \\ -\mu_+ n_+ \frac{\partial E}{\partial x} - v_d^+ \frac{\partial n_+}{\partial x} = n_{pair} - k_{MN} n_+ n_- - k_R n_+ n_e \\ -\mu_- n_- \frac{\partial E}{\partial x} - v_d^- \frac{\partial n_-}{\partial x} = k_A n_X n_e - k_{MN} n_+ n_- \\ \frac{\partial E}{\partial x} = \frac{1}{\epsilon}(n_+ - n_- - n_e) \end{cases} \tag{7}$$

where k_e is the recombination rate for electrons and Ar_2^+ ions. The final model plots are shown in figure 21. For the expected photon rate the mutual neutralization plays a major role, increasing its value of almost a factor 10.

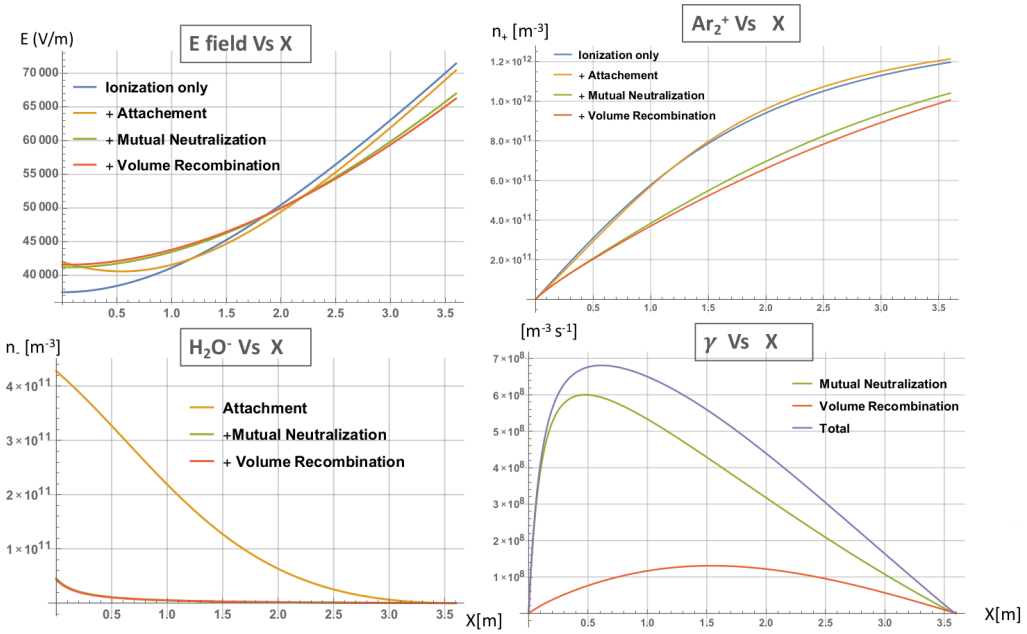

Figure 21: Complete solution of the model, including also the volume recombination. On bottom right the single photon generated by mutual neutralization and volume recombination.

Some additional variables are needed to correlate model and measurements, in particular it is possible tu study the single photon rate with respect to the electric field of the TPC and the purity of the liquid argon. The model prediction are shown in figure 22 on the following page. The photon rate decreases for higher electric field, while increases with the impurity concentration because of the mutual neutralization. In this model the light absorption is not taken into account.

4.3 Measure of SPR in ProtoDUNE

Measurement of the single photon rate in ProtoDUNE can give hints on the validity of the model. I developed a method in order to establish the single photon rate inside the detector and used it to point out the trend of the variable with respect to electric field, purity and time.

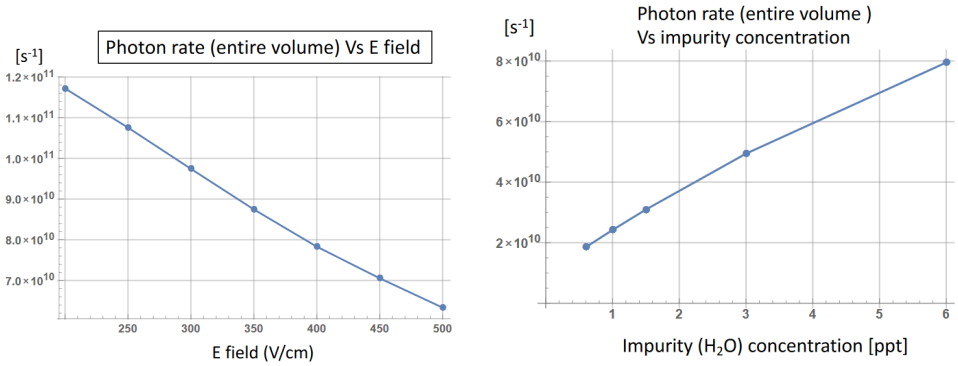

Figure 22: Photon rate with respect to TPC parameters. The single photon rate decreases with higher electric field (on the left) while it increases with the impurity concentration (in the right) because of the mutual neutralization. In the model the light absorption is not included.

4.3.1 Selection of events

The data analyzed are those coming from the ARAPUCA modules. This light detector is segmented in 16 cells with 12 output channels (figure 23 on the next page). Each of the first 8 cells contains 12 SiPMs and each cell is connected to a single output channel. The last 8 cells have only 6 SiPMs each and are connected to the output in couples. Each output channel has 12 SiPMs connected and the expected efficiency should be similar for every channel.

At each trigger the DAQ system reads the output of each channel and stores it in form of ROOT histograms. The first thing to do is to dump waveforms from the storage using the "LArSoft" software for the channels of interest. As a second step a preprocessing of waveforms is needed to extract relevant information from raw data (figure 24 on page 28).

- Filtering waveforms with a moving average algorithm
- Implementing a peak finder algorithm to get the position of the peak
- Extract time of the peak, peak height, waveform integral, channel and event number

At this point it is necessary to select events from space-charge recombination and to exclude those originated by ionizing particles. In the last case many photons are emitted at the same time, so there is a high probability that many channels are fired at the same time. So we can consider that

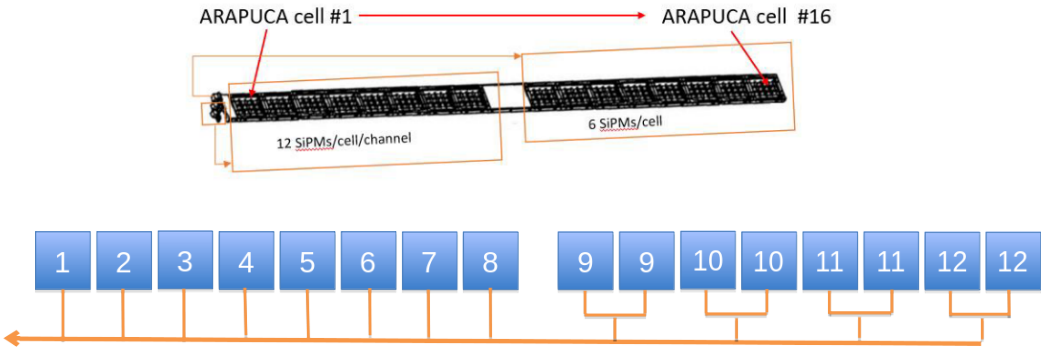

Figure 23: On the top an arapuca module with 16 cells. On the bottom the connection of the signals: the first 8 cells have a single output, while the last 8 are connected in couples. The first 8 cells have 12 SiPMs installed for each one, while the last 8 only 6 SiPMs. At the end each channel has 12 SiPMs connected.

ionizing events produce at least two channels triggering at the same time. On the other hand, events created by space charge neutralization are single photons that are emitted randomly in space and time. Imposing a coincidence window it is possible to exclude events that have 2 or more triggered channel in the same window. In this way only random single photon events are selected (figure 25 on the next page).

4.3.2 Rate estimation

The number of detected photons coming from true random single photons is distributed according to a poissonian distribution.

$$P(n;\nu) = e^{-\nu}\frac{\nu^n}{n!} \tag{8}$$

Considering the number of times that no photons are detected N_0 and the number of times we see photons N_{tot} the probability should be:

$$P(0;\nu) = \frac{N_0}{N_{tot}} = e^{-\nu} \tag{9}$$

thus ν photons are expected in each measurement window:

$$\nu = -\ln\frac{N_0}{N_{tot}} \tag{10}$$

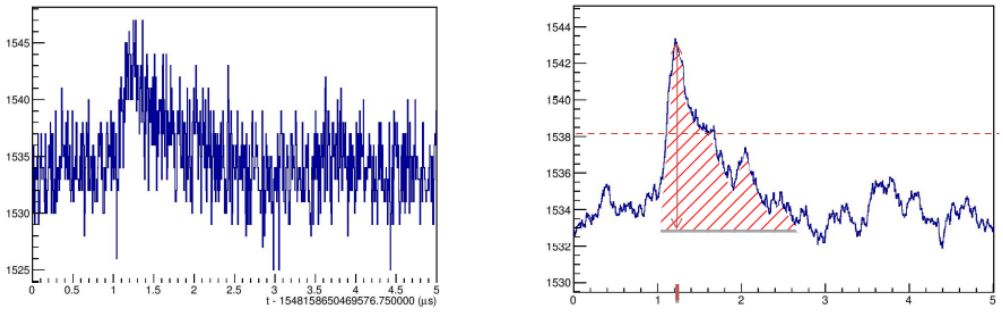

Figure 24: On the left a raw waveform of a single photon electron. On the right the filtered waveform with the indication of the peak height and the area of the signal.

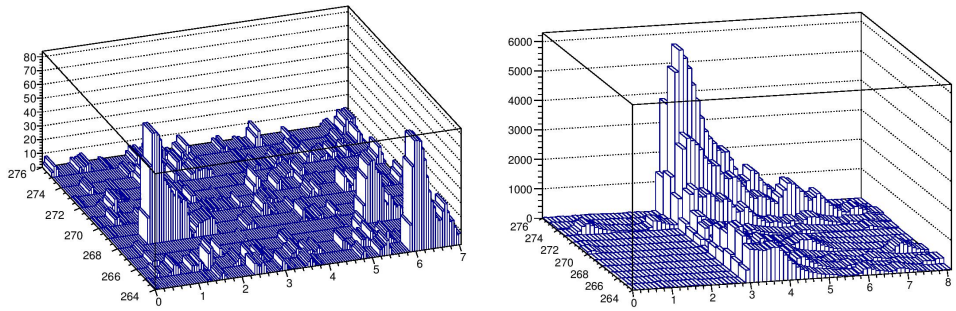

Figure 25: On the left three single photons that are uncorrelated. On the right an ionizing event in which all the channels are triggered at the same time.

The rate can be computed considering the time of measurement τ considered:

$$R = \frac{\nu}{\tau} \tag{11}$$

In figure 26 on the following page it is shown the distribution of the number of photons detected before the cut, after the cut and also the expected distribution for the measured rate. The first curve (blue) exhibits a long tail at high number of photons detected and it is due to ionizing events. After the cut (red curve) the tail is removed and the distribution resembles the expected one (green curve).

To efficiently exclude ionizing events it is necessary to optimize the coincidence window. As the events must be uncorrelated, the sum of the rates computed for each channel must be the same as the total rate.

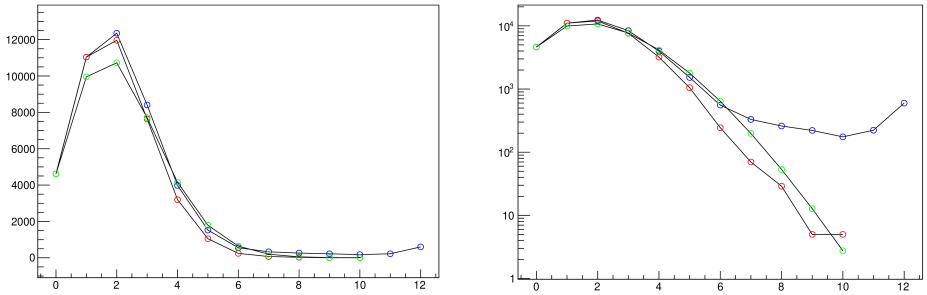

Figure 26: Photon distribution in linear (on the left) and logarithmic scale (on the right) for the ARAPUCA2. In blue the data without any selection, in red the data with the selection while in green the expected poissonian distribution. The ionizing events create a long tail for high number of photons that is removed by the selection.

$$\sum_i \nu_i = \nu \tag{12}$$

Thus minimizing the quantity Q defined in equation 13 it is possible to compute the optimum coincidence window. An example is shown in figure 27 on the following page for ARAPUCA 2, the optimum coincidence window is around 50 ns.

$$Q = \left(\sum_i \nu_i - \nu \right)^2 \tag{13}$$

4.4 Results

The analysis presented in the previous chapter has been performed on many runs. The goal is to understand the beahvior of the single photon rate with respect to the time, to evaluate the stabilty of the measure and the system, with respect to the electric field of the TPC and respect to the purity of the LAr.

In figure 28 on page 31 the rate is presented as a function of the electric field, for two different high voltage rampages, the first in November 2018 while the second in January 2019. The trend in the first plot is compatible with the expected one, thus the single photon rate decreases with a higher electric field. In the second plot a different behavior is shown in the ARAPUCA2. While the trend is always the same, the second arapuca seems to have an offset. This effect is still unexplained and could be due to changes in the setup that are not still clear.

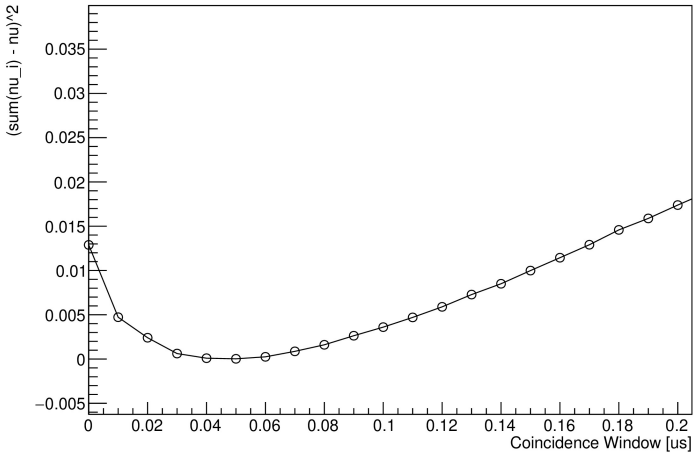

Figure 27: Optimization of the coincidence window for the ARAPUCA2. As the event are independent the sum of the rates of the single cells must be equal to the total rate. The optimum window is obtained minimizing equation 13 on the preceding page.

In figure 29 on the following page it is presented the single photon rate with respect to the level of purity, measured in electron lifetime units. In the plot on the left both ARAPUCA data are presented, while on the right there is the zoom for ARAPUCA2. It is possible to see that the single photon rate increases with the electron lifetime until it reaches a value around 7 ms. Thereafter the value seems to slightly decrease.

From the developed model, the single photon rate is expected to increase (opposite behavior of data) with the concentration of impurities because of the mutual neutralization process. On the other hand the model does not take into account the absorption rate induced by impurity molecules.

A possible explanation (figure 30 on page 32) can be given considering that a first increase of impurity concentration produce an increased rate, but the quenching and absorption mechanisms are not relevant before a fixed concentration. After a certain point ($\sim 1/7\,\mathrm{ms}^{-1}$) the limiting factor becomes the absorption of light, thus the rate decreases because of the latter.

To both understand the stability of the system and of the physical quantity, I have studied the variation on a timescale of 8 months. The trend does not show any variation, although some points are not consistent with the trend. This could be given by any external variation (purity, re-circulation,...) that was not considered, evaluated or written in the logbook.

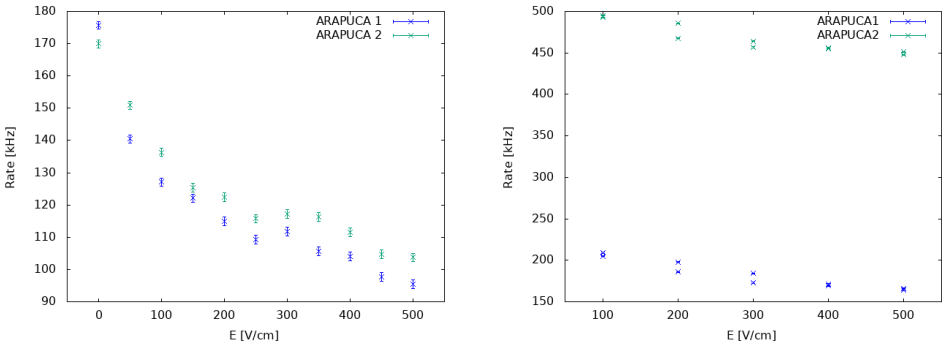

Figure 28: Single photon rate as a function of electric field. On the left the data for November 2018, on the right data for January 2019. On the right the ARAPUCA2 experience a much higher photon rate due to an offset. The trend is the same in both cases and is in good agreement with the model prediction.

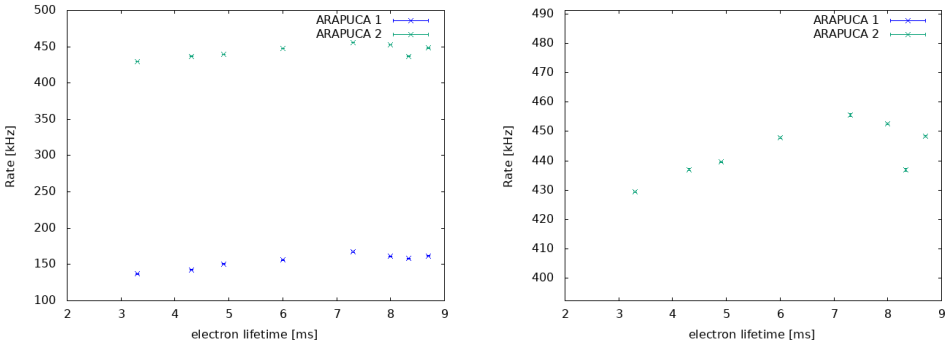

Figure 29: Single photon rate with respect to the purity. On the left the measure for ARAPUCA1 and ARAPUCA2. On the right the zoom for ARAPUCA2: the single photon rate increases with the purity level until 7 ms of electron lifetime, after that point it starts decreasing.

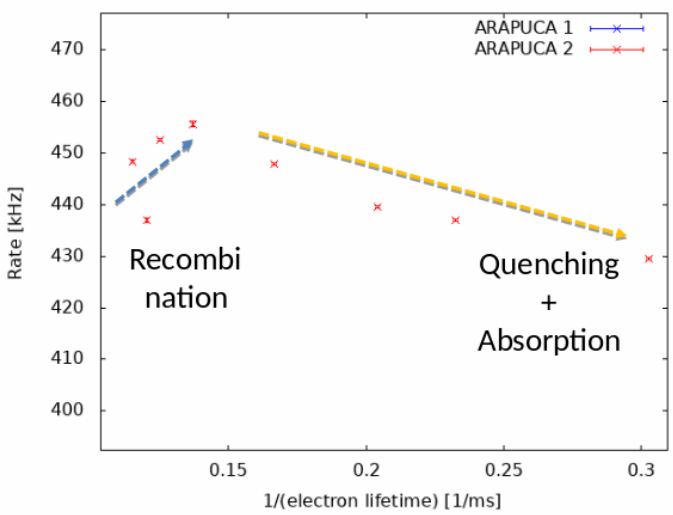

Figure 30: Interpretation of single photon rate with respect to purity. The increase of the single photon rate with the impurity concentration is the one expected, the decrease is due to quenching and absorption that is not included in the model.

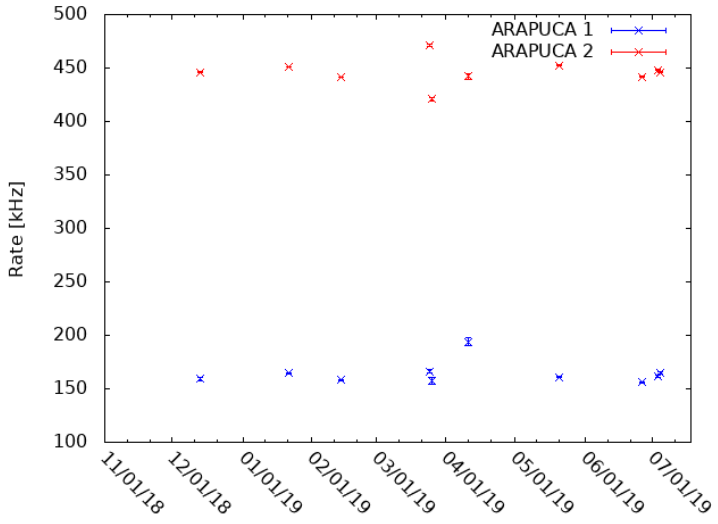

Figure 31: Single photon rate as a function of time: the variable is stable in time, no trend appears in 8 month of data taking.

5 Xenon Doping of LAr

5.1 Motivation

The simultaneous read-out of the charge and light signals in liquid noble gases detectors is an important tool for many experiments ranging from dark matter to large LArTPC. The light signal provides the much needed t_0 for nucleon dacays and supernova neutrinos and an enhanced light collection would allow for calorimetry and event position reconstruction. So far the light signal used (or planned to be used) comes from the VUV scintillation with wavelengths ranging from 78 nm (LNe) to 175 nm (LXe). Detection of VUV light presents many challenges:

- Use of WLS (wavelength shifters) with a long term stability that is not clear
- Complicated schemes for collecting the light
- Recent estimates of Rayleigh scattering length puts it at 55 cm [13] start having pernicious effects especially for extremely large LArTPCs (DUNE). This short value for the Rayleigh scattering length is indirectly confirmed by recent results from ArDM and DarkSide-50.
- Attention has been drawn recently to the possibility that the most commonly used WLS, TPB, might be soluble in LNGs [14].

Mixing Argon and Xenon in the gas phase has a long history going back to the 70s (laser physics, spectroscopy) [15]. These works found out very efficient *radiationless electronic energy transfer between electronically excited rare gas diatomic molecules and a rare gas atom of a different kind*. With this technique it is possible to convert the energy released in the Argon to excited states of Xenon. The Xenon emission light has a higher wavelength, thus easier to detect, the Rayleigh scattering is reduced and the deexcitation of Xe is very fast $\sim$ ns.

In the early 90's several groups examined doping LAr with varying concentrations of Xe. Some conclusions [16]:

- An admixture of 100 ppm Xe was found to produce complete wavelength shifting of the scintillation light from 218 nm to 178 nm [17].
- Adding Xe to Ar resulted in a progressive increase of scintillation light output, by up to a factor 2, for Xe concentrations up to 1%, in zero electric field, this increase being suppressed by electric fields from 1 kV cm^{-1} to 8 kV cm^{-1} [18].

- 3. The addition of only 100 ppm Xe produces considerable changes in scintillation pulse shape, including a small improvement in neutron/gamma pulse shape discrimination for only 300 ppm Xe [19] suggesting further investigation of pulse shape discrimination at larger Xe fractions.

TU Munich (Ulrich, Schoenertand various students and postdocs) published in 2014-15 new results obtained with a table-top setup (cubic centimeter volumes) and very intense, pulsed low energy beams (12 keV). Varying concentrations of Xe, controlling the purity of of the initial LAr with a sophisticated distillation technique. They look at a wide wavelength region from the VUV to the NIR.

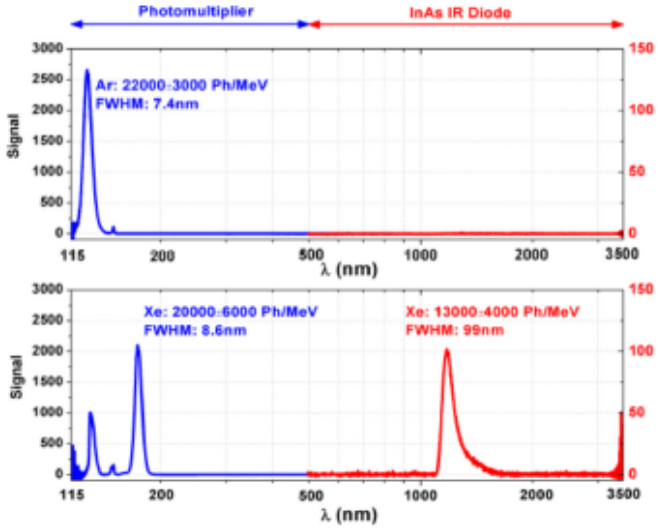

Figure 32: TUM results on xenon doping of liquid argon. On the top the emission of LAr scintillation light, on the bottom the emission with Xenon. Part of 128 nm light is shifted to 174 nm and a new infrared peak appears at 1180 nm.

They observed a shift from 128 nm to 174 nm and a strong emission in the infrared region at 1180 nm.

In 2016 the Indiana University group used the Blanche cryostat with the IU light guide bars as the photon detection system to investigate Xe doping of LAr. They also included NIR photodiodes and installed a NIR PMT on an observation window to look for the NIR light. The experiment showed twice more VUV light was seen at a concentration of 7 ppm and no NIR signals were present.

The result in the field are both interesting for their application and in contradiction one with the other. Experiments about this topic will be necessary to understand correctly the phenomena.

5.2 Experimental setup and goals

At Fermilab PAB facility an experiment to measure the light of LAr doped with Xe is going to be performed. The "Luke" cryostat will be used to control the cryogenics and the liquid argon. Inside this setup a small PTFE chamber will be installed, it has a cylindrical shape with a PMT coupled at the top (figure 33) and a SiPM will be installed on a face. The PMT is sensitive to the shifted 175 nm light of the liquid xenon, while the SiPM to the NIR light if present.

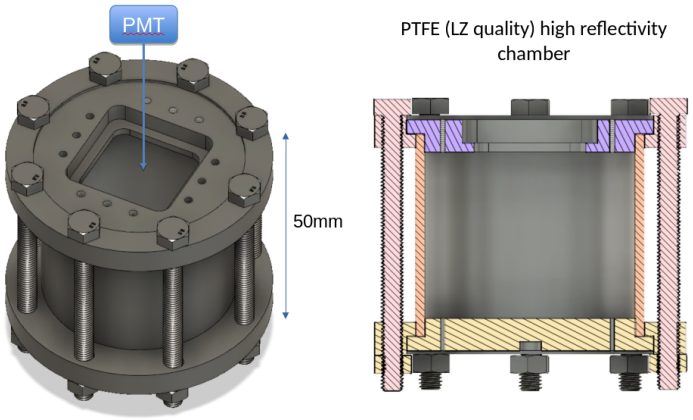

Figure 33: Chamber for xenon doping experiment at Fermilab. A cylinder made of PTFE (high reflectivity material) of LZ quality will be used to collect the light and guide it to a PMT (NUV region) that will be installed at the top. At the bottom a gamma source will be used to produce scintillation light.

Inside the cryostat some xenon will be injected to obtain a desired concentration and it will flow inside the chamber through some holes on top and bottom of the cylinder. Part of the xenon will be activated (^{137}Xe) and its emitted light will be monitored in order to evaluate the uniformity and stability of the doping.

At the bottom of the chamber a gamma source will be installed to measure the efficiency of the light shifting by xenon.

The main goal of this experiment is to quantify the efficiency of the shifting as a function of LXe concentration and to establish weather a NIR com-

ponent of the light is emitted in the process.

5.3 Reflection of light

A simulation for the reflection of light is needed to understand the response of the setup, in particular its uniformity and efficiency. To this end it is important to understand the phenomenology of the possible reflections of light. The main components that are present are: specular spike (SS), specular lobe (SL) and the diffuse lobe (D) (figure 34).

The specular spike component is given by the light that is reflected in a specular way with respect to the avarage normal of the surface. The specular lobe is the result of specular reflections of the microfacets of the surface that are distributed around the average one. The diffused light is caused by the photons that are scattered inside the first layer of the surface and riemitted in the volume.

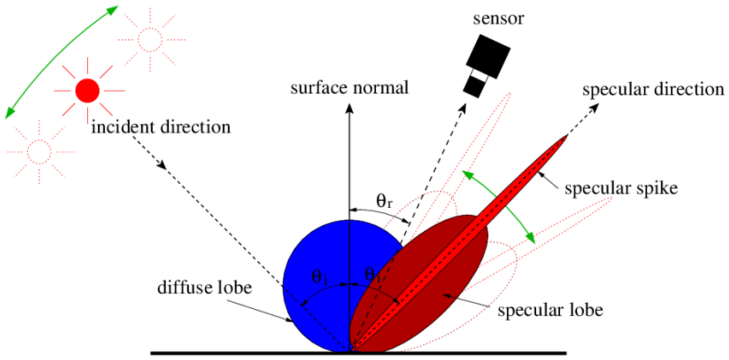

Figure 34: Reflection mechanisms: specular spike (reflection with respect to the average normal), specular lobe (specular reflection of micro-facets) and diffuse lobe (scattering of light in the first layers of the material).

Different models can describe these processes taking into account different properties of the material. In the model analyzed we can decompose the problem in describing the surface shape, thus fixing the distribution of the slopes of the microfacets and some geometrical factor that takes into account shadowing effects, and the physical model of the interaction of the photon with matter.

The first model considered is the one with no roughness [20], thus the surface is flat, in this case the probability of a photon to be reflected specurarly (SS-SL) is given by fresnel equation:

$$P_{specular} = \frac{1}{2}\left\{\frac{n^2\cos\theta_i - \sqrt{n^2-\sin^2\theta_i}}{n^2\cos\theta_i - \sqrt{n^2-\sin^2\theta_i}} + \frac{n^2 - \sqrt{n^2-\sin^2\theta_i}}{n^2 - \sqrt{n^2-\sin^2\theta_i}}\right\} \tag{14}$$

where it is considered the average of polarization and $n = n_{PTFE}/n_{LXe}$. The diffused component is assumed to be distributed according to a Lambertian distribution.

$$d\,P_{diff} = A\,(1 - P_{specular})\cos\theta_r d\,\theta_r \tag{15}$$

Where A represents the albedo, thus the integral probability that the photon is not absorbed but reflected.

Including the roughness means specifying the probability distribution of the angle between the average normal and that of the microfacet. Without loss of generality the equation [21] governing the reflection are:

$$\begin{cases}\rho_{SS} = \Lambda \times F(\theta_i, n)P(\alpha, \vec{\sigma})G(\alpha, \theta_i, \theta_r)\\ \rho_{SL} = (1-\Lambda) \times F(\theta_i, n)P(\alpha, \vec{\sigma})G(\alpha, \theta_i, \theta_r)\\ \rho_D = A \times (1 - F(\theta_i, n))(1 - F(\theta_r, 1/n))P(\alpha, \vec{\sigma})G(\alpha, \theta_i, \theta_r)\cos(\theta_r)\end{cases} \tag{16}$$

where ρ expressions are the probability distribution function for photon to undergo a fixed process (SS, SL and D). F functions are Fresnel equations, P is the distribution of the microfacets and G is the geometrical factor. The Λ factor is given by:

$$\Lambda = \exp - \left(\frac{4\pi n_0 \sigma_h \cos\theta_i}{\lambda}\right) \tag{17}$$

where σ_h is the standard deviation of microfacets height. In the simulation I consider $\sigma_h/\lambda \gg 1$ thus the SS process negligible.

The geometrical factor takes into account that photons can be stopped by the inclination of a nearby microfacets before arriving on the surface (shadowing) or that it is stopped after reflection (masking) as shown in figure 35 on the following page.

The two model chosen are the the Torrance-Sparrow and Trowbridge-Reitz. The microfacets distrubution are [21]:

$$P(\alpha, \sigma) = \frac{1}{\sqrt{2\pi}\sigma_\alpha}\exp\left(-\frac{\alpha^2}{2\sigma^2}\right) \qquad \text{Torrance-Sparrow} \tag{18}$$

$$P(\alpha, \gamma) = \frac{\gamma^2}{\pi\left(\gamma^2\cos^2\alpha + \sin^2\alpha\right)} \qquad \text{Trowbridge-Reitz} \tag{19}$$

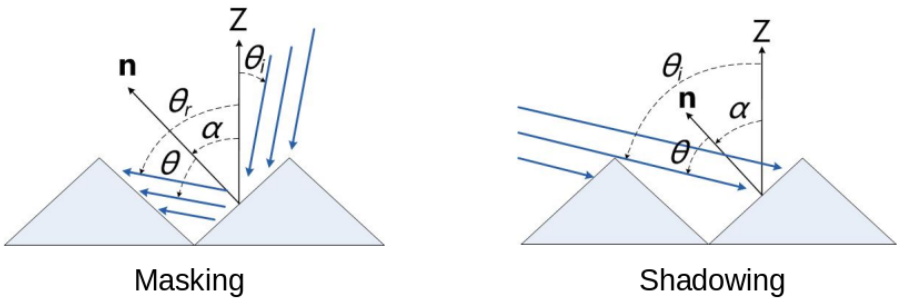

Figure 35: The geometrical factor $G(\alpha, \theta_i, \theta_r)$ describes the masking and shadowing effects of micro-facets. In the first case the reflected light is killed by a nearby surface deformation, while in the second case the impinging light is attenuated by a micro-facet that is near the point of reflection.

While the geometrical factors are:

$$G(\alpha, \theta_i, \theta_r) = \min\left\{1; \frac{2\cos\alpha\cos\theta_r}{\cos(\theta_r - \alpha)}; \frac{2\cos\alpha\cos\theta_i}{\cos(\theta_r - \alpha)}\right\} \quad \text{Torrance-Sparrow} \quad (20)$$

$$G(\alpha, \theta_i, \theta_r) = \frac{2}{1+\sqrt{1+\gamma^2\tan^2\theta_i}} \frac{2}{1+\sqrt{1+\gamma^2\tan^2\theta_r}} \quad \text{Trowbridge-Reitz} \quad (21)$$

5.4 Simulation

The montecarlo simulation is performed considering a uniform distribution of photons inside the volume of the chamber (figure 36 on the next page on left). Each initial photon has a direction of propagation that is isotropic (figure 36 on the following page on right).

After the generation the photons are propagated to the internal faces of the box through a ray-tracing algorithm. At this point the possible processes are evaluated. First the probability of specular reflection is computed $P_{specular}$ then a random number is generated $r \in [0, 1]$, if $r < P_{specular}$ the photon is reflected in a specular way. If not, the photon can undergo a diffusive reflection if it is not absorbed. At this point the code checks whether the photon is reflected considering the albedo A and if the answer is positive it will be propagated. The propagation ends when the photon is either absorbed or impinges on the photocathode surface.

From the computational point of view, each photon is described by a class that contains its position and direction.

```
class event{
private:
```

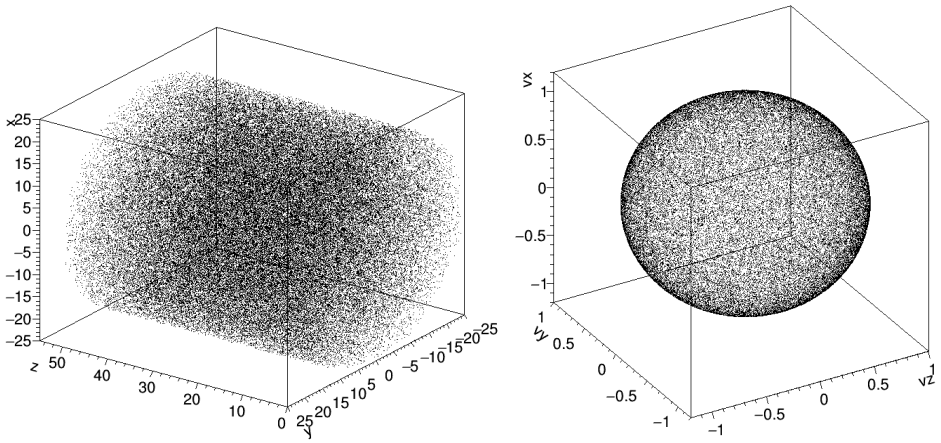

Figure 36: Simulation: on the left the distribution of the generated photons, on the right the distribution of their direction of propagation.

```
  TVector3 _pos;
  TVector3 _dir;
public:
  event() {
    for(int i=0; i<3; i++){
        _pos[i] = 0;
        _dir[i] = 1/sqrt(3);
        }
  }

  event(TVector3 pos, TVector3 dir){
    _pos = pos;
    _dir = dir;
  }

  event(TVector3 pos, double unif1, double unif2) {
    _pos = pos;
    double theta = 2 * M_PI * unif1;
    double phi = acos(1 - 2 * unif2);
    double x = sin(phi) * cos(theta);
    double y = sin(phi) * sin(theta);
    double z = cos(phi);
    _dir[0] = x;
    _dir[1] = y;
    _dir[2] = z;
```

```
    }

    TVector3 get_pos(){return _pos;}
    TVector3 get_dir(){return _dir;}
    event(event & ev){
    _pos = ev.get_pos();
    _dir = ev.get_dir();
    }

    void set_pos(TVector3 pos){_pos = pos;}
    void set_dir(TVector3 dir){_pos = dir;}

    event& operator= (const event& ev){
    this->_pos = ev._pos;
    this->_dir = ev._dir;
    return *this;
    }

    ~event(){}
};
```

The setup is described in a class called cylinder. It contains dimensions and physical parameters on reflections. It implements the geometry, ray-tracing and the different surface models that are used in the simulation.

```
class cylinder{
private:
  double _R;
  double _h;
  double _refl;
  double _n;
  double _wx;
  double _wy;
public:
  cylinder(){
    _R=1;
    _h=1;
    _refl=1;
    _n=1;
    _wx=1;
    _wy=1;
  }
```

```
  cylinder(double R, double h, double refl, double n
     , double wx, double wy);

  TVector3 uniform_position(TVector3 uniform);

  event get_next_event(event ev, double unif1,
     double unif2, double unif3);

  event get_next_event_Torrance_Sparrow(event ev,
     double sigma, double unif1, double unif2,
     double unif3, double unif4, double unif5);

  event get_next_event_Towbridge_Reitz_Wolff(event
     ev, double gamma, std::mt19937 &generator);

  ~cylinder();
};
```

5.5 Results

The simulation generates 1×10^6 photons, and the uniformity is evaluated considering the photons that reach the photocathode from a given (x, y, z) point. In figure 37 on the next page it is presented the cylinder in a top view, the color scale indicates the number of photons that reached the PMT window from a (x, y) position regardeless of the z coordinate. In this plot we can establish the uniformity on the $x-y$ plane of the illumination for different roughness parameters, in particular these plots refer to the Trowbridge-Reitz model [22].

In figure 38 on page 43 it is presented the cylinder from a side view, it is shown the uniformity on the $x - z$ plane for different values of the roughness parameter in the Trowbridge-Reitz model. In both sights the uniformity decreases with a higher roughness of the surface.

At the end I have computed the collection efficiency for the three models with respect to the roughness parameter. In figure 39 on page 44 the results are shown, the flat solution is not dependent on the roughness since is the model for flat surface. The region in which we are interested [23] is between 0 and 0.1. The discontinuity in zero is due to the approximation $\sigma_h/\lambda \gg 1$ that fails nearby low values of the parameter. With this consideration we expect to have an optimum roughness, since for low values of σ_h the deformation

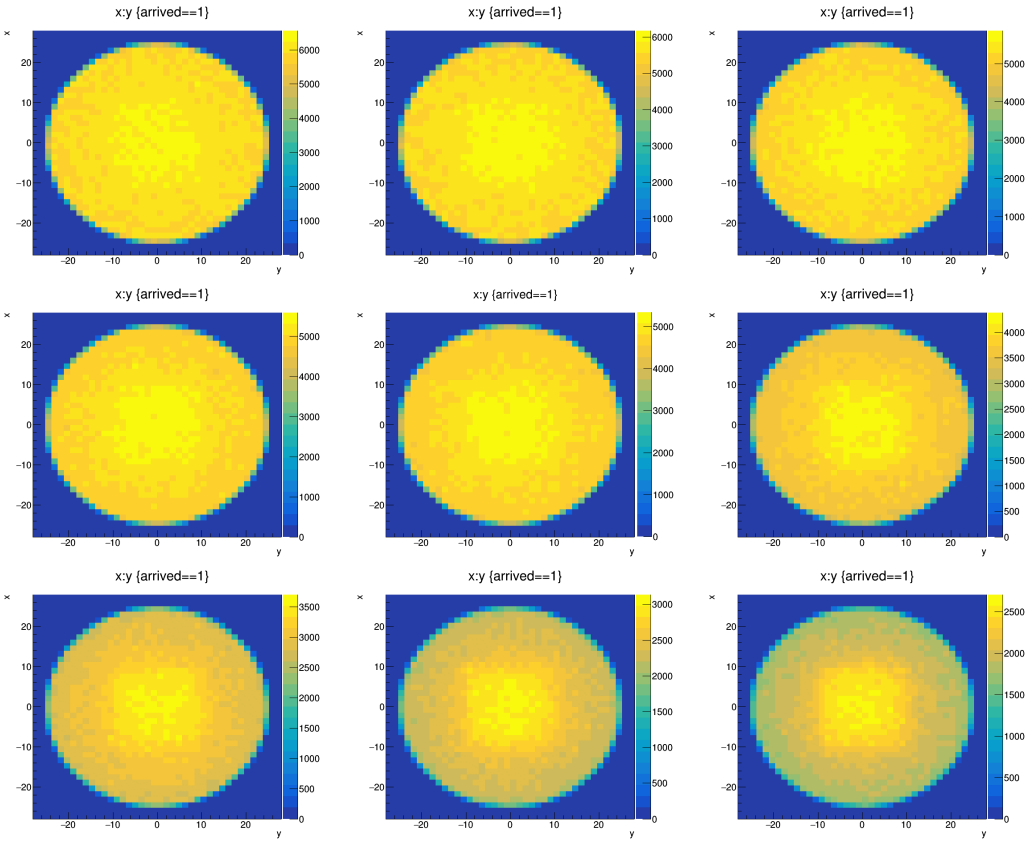

Figure 37: Top view of the cylinder. Plot of the points (x, y) where collected photons were generated. The uniformity decreases with higher roughness. The parameter for each image is $\sigma = \{0.02, 0.04, 0.06, 0.08, 0.1, 0.2, 0.3, 0.4, 0.5\}$.

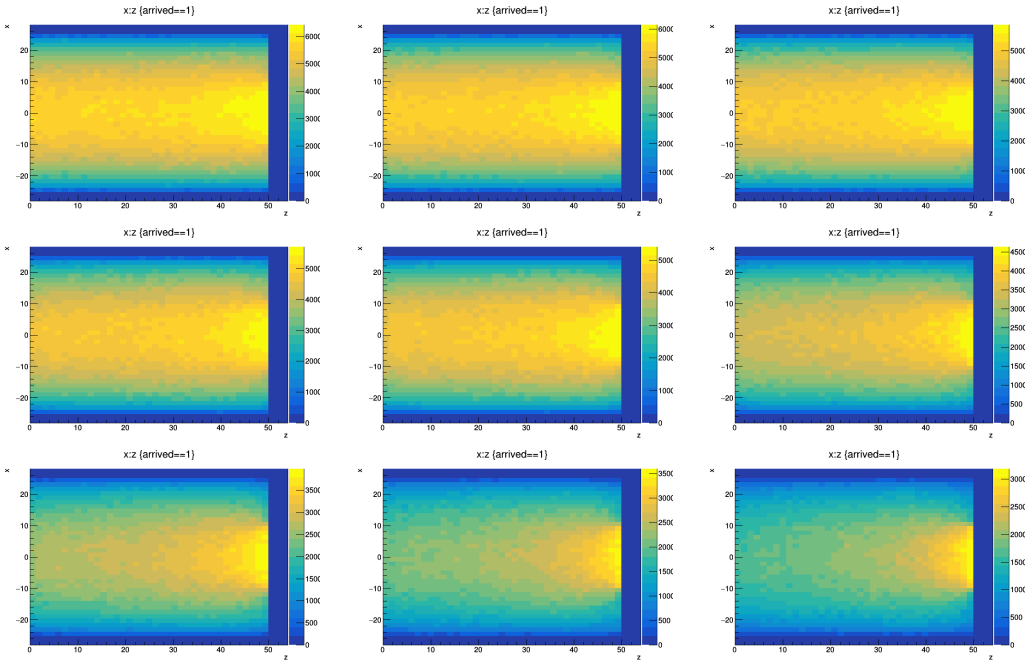

Figure 38: Side view of the cylinder. Plot of the points (z, x) where collected photons were generated. The uniformity decreases with higher roughness. The parameter for each image is $\sigma = \{0.02, 0.04, 0.06, 0.08, 0.1, 0.2, 0.3, 0.4, 0.5\}$.

of the surface helps the diffusion of the light, while after a ceratin point the geometrical factor kills the light.

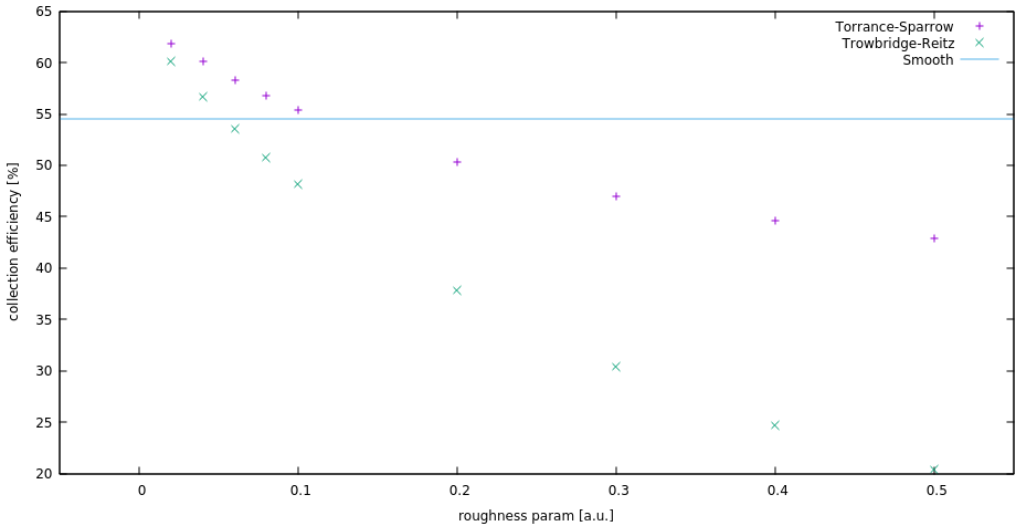

Figure 39: Collection efficiency for three different models with respect to the relative roughness parameter. The flat solution relates to the "smooth surface" model. The discontinuity in 0 is due to the approximation $\sigma_h/\lambda \gg 1$ that is not valid for low values of roughness. Thus an "optimum" roughness for the collection efficiency is expected.

Tu evaluate the response of xenon emission we considered the gamma energy around 30 keV. The expected photons generated at each interaction are $n_{ph} = LY \times E_\gamma \times \epsilon_{Xe}$ where ϵ_{Xe} is the energy transfer efficiency between Ar and Xe. Therefore in the simulation I considered a poissonian distribution for the number of photons with parameter $\nu = 40 \times 30 \times \epsilon_{Xe}$. The efficiency depends on the concentration, and the values used are shown in table 1.

Xe [ppm]	0	10	20	50	100	200	500	800	1000
ϵ_{Ar}	1	0.65180	0.51959	0.37663	0.30553	0.25872	0.21324	0.19015	0.17842
ϵ_{Xe}	0	0.34819	0.48041	0.62337	0.69446	0.74128	0.78676	0.80985	0.82158

Table 1: Emitted light for different concentration of liquid xenon in liquid argon. ϵ_{Ar} is the fraction of light emitted by LAr at 128 nm while the ϵ_{Xe} is the fraction emitted by LXe at 174 nm.

The expected distributions are thus plotted in figure 40 on the next page with respect to the number of photons collected.

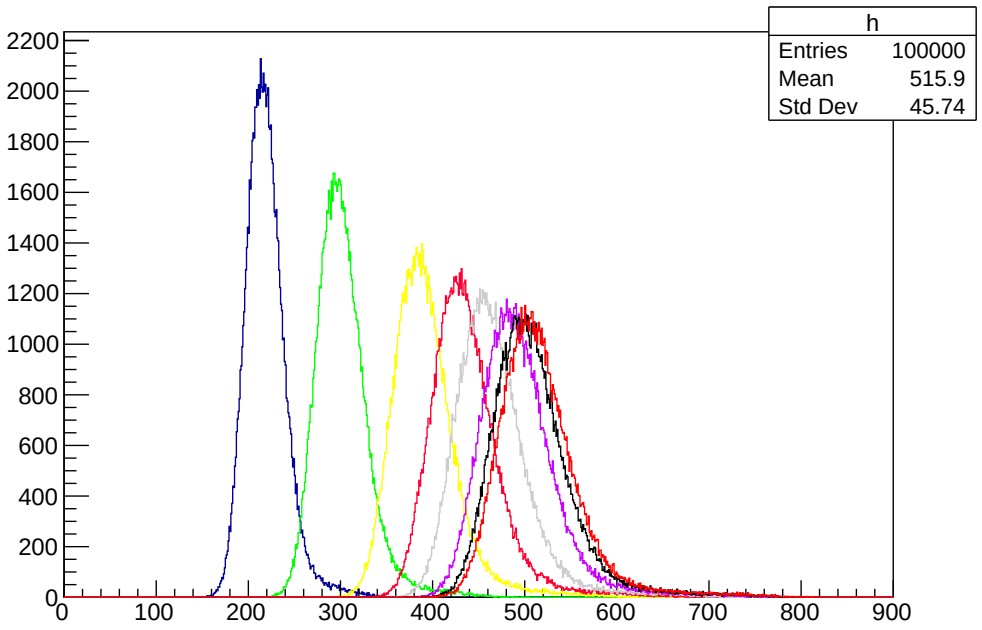

Figure 40: Distribution of collected photons for different concentration of liquid xenon: 10 ppm (blue), 20 ppm (green), 50 ppm (yellow), 100 ppm (red), 200 ppm (grey), 500 ppm (purple), 800 ppm (black), 1000 ppm (brown).

References

[1] DUNE Collaboration, B. Abi, R. Acciarri, M. A. Acero, M. Adamowski, C. Adams, *et al.*, "The DUNE Far Detector Interim Design Report, Volume 2: Single-Phase Module," *arXiv e-prints*, p. arXiv:1807.10327, Jul 2018.

[2] DUNE Collaboration, B. Abi, R. Acciarri, M. A. Acero, M. Adamowski, C. Adams, *et al.*, "The DUNE Far Detector Interim Design Report Volume 1: Physics, Technology and Strategies," *arXiv e-prints*, p. arXiv:1807.10334, Jul 2018.

[3] I. Esteban, M. C. Gonzalez-Garcia, M. Maltoni, I. Martinez-Soler, and T. Schwetz, "Updated fit to three neutrino mixing: exploring the accelerator-reactor complementarity," *Journal of High Energy Physics*, vol. 2017, p. 87, Jan 2017.

[4] P. Langacker, "Grand unified theories and proton decay," *Physics Reports*, vol. 72, no. 4, pp. 185 – 385, 1981.

[5] P. Nath and P. F. Pérez, "Proton stability in grand unified theories, in strings and in branes," *Physics Reports*, vol. 441, no. 5, pp. 191 – 317, 2007.

[6] W. D. Boer, "Grand unified theories and supersymmetry in particle physics and cosmology," *Progress in Particle and Nuclear Physics*, vol. 33, pp. 201 – 301, 1994.

[7] H. Nishino, K. Abe, Y. Hayato, T. Iida, M. Ikeda, *et al.*, "Search for nucleon decay into charged antilepton plus meson in super-kamiokande i and ii," *Phys. Rev. D*, vol. 85, p. 112001, Jun 2012.

[8] A. Mirizzi, I. Tamborra, H.-T. Janka, N. Saviano, K. Scholberg, *et al.*, "Supernova Neutrinos: Production, Oscillations and Detection," *Riv. Nuovo Cim.*, vol. 39, no. 1-2, pp. 1–112, 2016.

[9] K. Scholberg, "Supernova signatures of neutrino mass ordering," *Journal of Physics G: Nuclear and Particle Physics*, vol. 45, p. 014002, dec 2017.

[10] L. Hüdepohl, B. Müller, H.-T. Janka, A. Marek, and G. G. Raffelt, "Neutrino signal of electron-capture supernovae from core collapse to cooling," *Phys. Rev. Lett.*, vol. 104, p. 251101, Jun 2010.

[11] B. Abi, R. Acciarri, M. A. Acero, M. Adamowski, C. Adams, *et al.*, "The Single-Phase ProtoDUNE Technical Design Report," *arXiv e-prints*, p. arXiv:1706.07081, Jun 2017.

[12] A. Machado and E. Segreto, "ARAPUCA a new device for liquid argon scintillation light detection," *Journal of Instrumentation*, vol. 11, pp. C02004–C02004, feb 2016.

[13] E. Grace, A. Butcher, J. Monroe, and J. A. Nikkel, "Index of refraction, rayleigh scattering length, and sellmeier coefficients in solid and liquid argon and xenon," 2015.

[14] P. Sanguino, F. Balau, A. M. Rego, A. Pereira, and V. Chepel, "Stability of tetraphenyl butadiene thin films in liquid xenon," *Thin Solid Films*, vol. 600, 01 2016.

[15] A. Gedanken, J. Jortner, B. Raz, and A. Szöke, "Electronic energy transfer phenomena in rare gases," *The Journal of Chemical Physics*, vol. 57, no. 8, pp. 3456–3469, 1972.

[16] K. Arisaka, P. Beltrame, C. Lam, P. Smith, C. Ghag, D. Cline, K. Lung, Y. Meng, E. Pantic, P. Scovell, and et al., "Studies of a three-stage dark matter and neutrino observatory based on multi-ton combinations of liquid xenon and liquid argon detectors," *Astroparticle Physics*, vol. 36, p. 93–122, Aug 2012.

[17] E. Conti, G. Carugno, and A. Intravaia, "Time behaviour of the scintillation light in mixtures of liquid argon and xenon," *Nuclear Instruments and Methods in Physics Research Section A: Accelerators, Spectrometers, Detectors and Associated Equipment*, vol. 382, no. 3, pp. 475 – 478, 1996.

[18] M. Suzuki, M. Hishida, J. Ruan(Gen), and S. Kubota, "Light output and collected charge in xenon-doped liquid argon," *Nuclear Instruments and Methods in Physics Research Section A: Accelerators, Spectrometers, Detectors and Associated Equipment*, vol. 327, no. 1, pp. 67 – 70, 1993.

[19] P. Peiffer, T. Pollmann, S. Schönert, A. Smolnikov, and S. Vasiliev, "Pulse shape analysis of scintillation signals from pure and xenon-doped liquid argon for radioactive background identification," *Journal of Instrumentation*, vol. 3, pp. P08007–P08007, aug 2008.

[20] F. Neves, A. Lindote, A. Morozov, V. Solovov, C. Silva, P. Bras, J. Rodrigues, and M. Lopes, "Measurement of the absolute reflectance of

polytetrafluoroethylene (ptfe) immersed in liquid xenon," *Journal of Instrumentation*, vol. 12, p. P01017–P01017, Jan 2017.

[21] C. Silva, *Study of the Reflectance Distributions of Fluoropolymers and Other Rough Surfaces with Interest to Scintillation Detectors*. PhD thesis, Universidade De Coimbra, 2009.

[22] S. Kravitz, R. J. Smith, L. Hagaman, E. P. Bernard, D. N. McKinsey, L. Rudd, L. Tvrznikova, G. D. O. Gann, and M. Sakai, "Measurements of angle-resolved reflectivity of ptfe in liquid xenon with ibex," 2019.

[23] C. Silva, J. Pinto da Cunha, A. Pereira, M. Lopes, V. Chepel, V. Solovov, and F. Neves, "A model of the reflection distribution in the vacuum ultra violet region," *Nuclear Instruments and Methods in Physics Research Section A: Accelerators, Spectrometers, Detectors and Associated Equipment*, vol. 619, p. 59–62, Jul 2010.